Clean Energy, 2023, Vol. 7, No. 1, 157–173
https://doi.org/10.1093/ce/zkad006
Advance access publication 10 March 2023
Research Article

Wind-farm and hydrogen-storage co-location system optimization for dynamic frequency response in the UK

Fulin Fan[1,*], Shanay Skellern[1], David Campos-Gaona[1] and John Nwobu[2]

[1]Department of Electronic and Electrical Engineering, University of Strathclyde, Glasgow, UK
[2]Offshore Renewable Energy Catapult, Glasgow, UK
*Corresponding author. E-mail: f.fan@strath.ac.uk

Abstract

The continuous development of hydrogen-electrolyser and fuel-cell technologies not only reduces their investment and operating costs but also improves their technical performance to meet fast-acting requirements of electrical grid balancing services such as frequency-response services. In order to project the feasibility of co-locating a hydrogen-storage system with a wind farm for the dynamic regulation frequency-response provision in Great Britain, this paper develops a modelling framework to coordinate the wind export and frequency responses to the main grid and manage the interaction of the electrolyser, compressor, storage tank and fuel cell within the hydrogen-storage system by respecting the market mechanisms and the balance and conversion of power and hydrogen flows. Then the revenue of frequency-response service provision and a variety of costs induced by the hydrogen-storage system are translated into the net profit of the co-location system, which is maximized by optimizing the capacities of hydrogen-storage-system components, hydrogen-storage levels that guide the hydrogen restoration via operational baselines and the power interchange between a wind-farm and hydrogen-storage system, as well as the capacities tendered for low- and high-frequency dynamic regulation services. The developed modelling framework is tested based on a particular 432-MW offshore wind farm in Great Britain combined with the techno-economics of electrolysers and fuel cells projected for 2030 and 2050 scenarios. The optimized system configuration and operation are compared between different operating scenarios and discussed alongside the prospect of applying hydrogen-storage systems for frequency-response provision.

Graphical Abstract

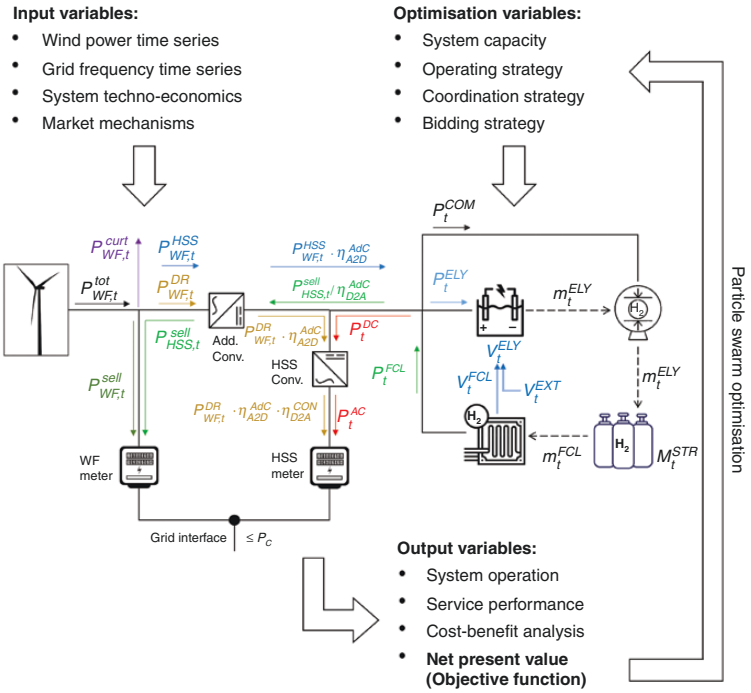

Keywords: dynamic regulation frequency response; hydrogen-storage system; techno-economic optimization; UK perspective; wind farm

Received: 3 October 2022. **Accepted:** 17 January 2023

Introduction

Low-carbon hydrogen (H_2) is considered to play a vital role in the decarbonization of different energy sectors [1]. More than 95% of the global H_2 supply is currently produced from fossil fuels, especially via the steam-methane reforming process [2]. Though being an economical method of H_2 production, steam reforming will create carbon dioxide as one of main by-products and can be equipped with carbon capture and storage facilities to reduce carbon emissions [3]. The remaining global H_2 supply is mainly met by the water-electrolysis process that consumes electricity to split water into H_2 and oxygen without the release of polluting by-products [4]. Although water electrolysis requires greater investments than steam reforming, the combination of high electrolyser utilization rates with low-cost electricity from renewables can help increase the cost-effectiveness of H_2 production by electrolysis [2].

In addition to producing H_2 from renewable generation [5], water electrolysis has been receiving increasing interest in providing ancillary services (e.g. frequency response and reserve services) to electrical grids by varying the electrolysis import in response to the imbalance between generation and demand on the grids [6]. This can not only increase the flexibility of electrical grids to deal with the increasing integration of renewable generation, but also brings additional revenue streams to electrolyser owners from ancillary service markets. The ability of electrolysers to deliver ancillary services depends on technical requirements by the services of interest such as start-up time, operating range and ramping capability. To illustrate, experimental tests reported in [7] showed that a 40-kW polymer electrolyte membrane (PEM) electrolyser could be ramped up/down by 25–75% of its capacity in ~0.2 seconds, which is good enough to provide frequency-response services, though this ramping capability could be heavily affected by the balance-of-system and control strategies employed. The test protocols for qualifying PEM electrolysers to the European primary and secondary reserve markets were designed in [8], indicating that PEM electrolysers had the capability of satisfying the most stringent grid constraints. The performance of alkaline and PEM electrolysers ranging from 10 to 300 kW has been characterized for the frequency restoration reserve in Europe through the QualyGridS project [9], which suggested replacing the DC-current-following controller within the AC/DC converter by an active-power-following controller to address a certain time delay in the electrolyser import on the AC grid side. Furthermore, sub-second responses of electrolysers were achieved by modifying the factory-installed electrolyser control system [10] or developing a front-end controller [11], respectively, which verified the dynamics of electrolysers for grid support. Although alkaline and PEM electrolysers have shown their ability to meet the fast response requirements of ancillary services, their demonstration projects are still required to acquire the experience and knowledge of operating electrolysers for grid balancing in the field [12].

Besides fulfilling the technical requirements of ancillary services, the economic feasibility of developing an electrolyser project for grid balancing must be evaluated in advance. Most of the business models developed for electrolyser projects stack the ancillary service provision with additional revenue streams that exploit the value of H_2 production in different sectors [12–15]. The role of electrolysers in the revenue stacking of grid service provision and cross-commodity arbitrage trading between electricity and transportation, industry or natural-gas sectors was investigated in [13], which identified the profitability for transportation sectors. Furthermore, the techno-economic operation of an electrolyser system participating in the Spanish secondary regulation market at the same time as supplying H_2 to fuel-cell electric vehicles was modelled in [12], demonstrating that the ancillary service provision could contribute to the total profitability of the electrolyser project. The provision of the European frequency containment and restoration reserve services by the electrolyser systems that were located within H_2 refuelling stations was explored in [14] and [15], with the optimal sizes and dispatch schedules of H_2 refuelling stations being determined from an economic optimization perspective. In addition, considering that PEM fuel cells would share comparable technical capabilities to PEM electrolysers in the future, the prospect of fuel cells in ancillary service markets was assessed in [16] and [17], respectively. Although the expense of external H_2 supply could make it difficult to develop a profitable independent fuel-cell system based on a case study implemented in Denmark [16], the combination of electrolysers and fuel cells was evaluated to be economically viable in the European frequency reserve markets [17].

The contribution of this paper is to perform an optimization-based assessment on the feasibility of developing an onshore hydrogen-storage system (HSS) which combines a PEM electrolyser and a fuel cell to provide the latest end-state frequency-response services in Great Britain based on the techno-economics of the electrolyser and the fuel cell projected for 2030 and 2050. Specifically, the HSS is co-located with an offshore wind farm and shares the existing onshore connection point to provide frequency-response services to the main grid, making more efficient use of the existing infrastructure. A set of operating strategies are particularly designed to guide the interaction of HSS components (including electrolyser, compressor, storage tank and fuel cell) and their coordination with the wind farm while respecting the frequency-response market mechanisms and the physical balance of power, H_2 and water flows within the co-location system. Then the techno-economic characteristics of the HSS together with the operating strategies are integrated with a modelling framework to simulate the co-location system operation and the resulting net present value (NPV) at the end of a 15-year project lifespan. From an economic optimization perspective, the modelling framework is combined with a particle swarm optimization (PSO) method to maximize the NPV of the co-location project by optimizing the capacities of multiple HSS components, the contracted capacities of frequency-response services and H_2 storage-related strategy variables that guide the storage restoration via operational baselines and the power interchange between the wind farm and HSS, respectively. The techno-economics of the optimized co-location systems provide wind-farm owners in Great Britain with insights into the operation and feasibility of co-locating an HSS for frequency-response service provision in future circumstances, as well as the impacts of future technical improvement and cost reductions of PEM electrolysers and fuel cells on the co-location system optimization.

The paper is structured as follows. Section 1 describes the technical modelling of wind-farm and HSS co-location systems for frequency-response service provision; Section 2 details the costs and revenue streams of co-location systems and the PSO implementation; Section 3 discusses the optimization results and associated profits of co-location systems under different operating scenarios; and conclusions and recommendations for further work are presented in Section 4.

1 Technical modelling of wind-farm and HSS co-location systems

1.1 Onshore HSS modelling

An onshore HSS consisting of PEM electrolyser, compressor, storage tank, PEM fuel cell and AC/DC converter (see Fig. 1) is

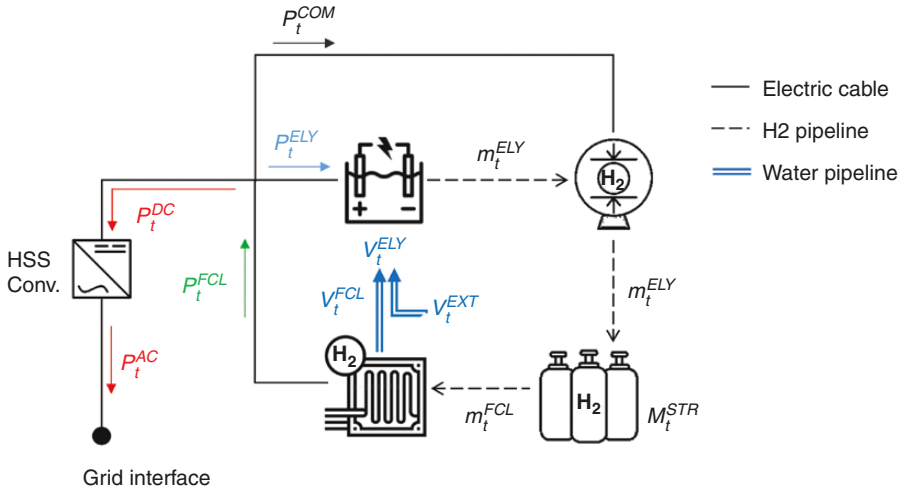

Fig. 1: Schematic of an onshore HSS with power, H_2 and water flows.

simulated here by formulating the balance of power, H_2 and water flows as well as their mutual conversion (see Equations (1–5), respectively). The bidirectional HSS converter connects the AC grid interface with the DC link of the HSS. Since this paper mainly deals with the dispatch of AC power flows within co-location systems, the DC/DC converters that integrate the electrolyser and the fuel cell with the DC link [18] are neglected in the modelling. The capture of oxygen produced by the electrolyser for reuse or other applications is also outside the scope of this work.

$$P_t^{FCL} - \left(P_t^{ELY} + P_t^{COM}\right) = P_t^{DC} = \begin{cases} P_t^{AC}/\eta_{D2A}^{CON}, & \forall P_t^{AC} \geq 0 \\ P_t^{AC} \cdot \eta_{A2D}^{CON}, & \forall P_t^{AC} < 0 \end{cases} \quad (1)$$

$$M_t^{STR} = M_{t-1}^{STR} + (m_t^{ELY} - m_t^{FCL}) \cdot \Delta t, \text{ with } M_0^{STR} = \overline{M}^{STR}/2 \quad (2)$$

$$v_t^{EXT} = \mathbb{N}\left\{\sum_{i=1}^{t}\left(v_i^{ELY} - v_i^{FCL} - v_{(i-1)}^{EXT}\right)\right\}, \text{ with } v_0^{EXT} = 0 \quad (3)$$

$$m_t^{ELY} = P_t^{ELY} \cdot \eta_{P2m,t}^{ELY} = v_t^{ELY} \cdot \eta_{v2m,t}^{ELY} \quad (4)$$

$$m_t^{FCL} = P_t^{FCL}/\eta_{m2P,t}^{FCL} = v_t^{FCL}/\eta_{m2v,t}^{FCL} \quad (5)$$

where P_t^{FCL}, P_t^{ELY}, P_t^{COM}, P_t^{DC}, and P_t^{AC} are the power export/import (MW) of the fuel cell, electrolyser, compressor and their aggregates on DC and AC sides at time step t, respectively; and η_{D2A}^{CON} and η_{A2D}^{CON} are the DC-to-AC and AC-to-DC conversion efficiencies of the HSS converter, which are assumed here to equal 95%. Terms M_t^{STR} and M_{t-1}^{STR} are the H_2 mass (kg) stored in the storage tank at t and $(t-1)$, with their difference being determined by the integrals of the H_2 production rate m_t^{ELY} (kg/h) of the electrolyser and the H_2 consumption rate m_t^{FCL} (kg/h) of the fuel cell over the time-step length Δt. The initial H_2 mass M_0^{STR} available in the storage tank is assumed to be half of the storage-tank capacity $\overline{M}^{STR}$ (kg). The operator $\mathbb{N}\{\cdot\}$ forces negative inputs to zero without affecting positive inputs in Equation (3), ensuring that an external freshwater source will supply at a rate of v_t^{EXT} (m^3/h) to make up for the freshwater shortage at t, which is estimated based on historic freshwater consumed by the electrolyser at rates of v_i^{ELY}, generated by the fuel cell at rates of v_i^{FCL}, and imported from the external source at rates of $v_{(i-1)}^{EXT}$ (i = 1,…,t). The conversion between H_2, power and freshwater at the electrolyser and the fuel cell are depicted by Equations (4) and (5), respectively. The power–H_2 and water–H_2 conversion efficiencies, denoted by $\eta_{P2m,t}^{ELY}$ (kg/MWh) and $\eta_{v2m,t}^{ELY}$ (kg/m^3) for the electrolyser and $\eta_{m2P,t}^{FCL}$ (MWh/kg) and $\eta_{m2v,t}^{FCL}$ (m^3/kg) for the fuel cell, are assumed here to linearly decline with time due to the stack degradation [12, 19]. Furthermore, the efficiencies of the electrolyser and the fuel cell are presumed to drop to 90% of their respective nominal levels (i.e. $\overline{\eta}_{P2m}^{ELY}$ and $\overline{\eta}_{v2m}^{ELY}$ for the electrolyser and $\overline{\eta}_{m2P}^{FCL}$ and $\overline{\eta}_{m2v}^{FCL}$ for the fuel cell) at the end of the stack lifetime (i.e. T_{Life}^{ELY} and T_{Life}^{FCL} for the electrolyser and the fuel cell, respectively) [12, 19] and then return to the nominal levels by the stack replacement that could occur multiple times depending on the co-location project lifespan. The changes of power–H_2–water conversion efficiencies with the time-dependent stack degradation and replacement are described by Equations (6–9):

$$\eta_{m2P,t}^{ELY} = \overline{\eta}_{m2P}^{ELY} \cdot \left[100\% - 10\% \cdot \mathrm{mod}(t \cdot \Delta t/T_{Life}^{ELY},\ 1)\right] \quad (6)$$

$$\eta_{m2v,t}^{ELY} = \overline{\eta}_{m2v}^{ELY} \cdot \left[100\% - 10\% \cdot \mathrm{mod}(t \cdot \Delta t/T_{Life}^{ELY},\ 1)\right] \quad (7)$$

$$\eta_{P2m,t}^{FCL} = \overline{\eta}_{P2m}^{FCL} \cdot \left[100\% - 10\% \cdot \mathrm{mod}(t \cdot \Delta t/T_{Life}^{FCL},\ 1)\right] \quad (8)$$

$$\eta_{v2m,t}^{FCL} = \overline{\eta}_{v2m}^{FCL} \cdot \left[100\% - 10\% \cdot \mathrm{mod}(t \cdot \Delta t/T_{Life}^{FCL},\ 1)\right] \quad (9)$$

To reduce the volume of H_2 at storage, the H_2 produced by the electrolyser at a low pressure b_{out}^{ELY} (bar) must be pressurized to a high pressure b_{in}^{STR} (bar) and stored in the storage tank. The power P_t^{COM} used by the compressor to pressurize H_2 from its inlet pressure b_{in}^{COM} to outlet pressure b_{out}^{COM} is calculated as a product of m_t^{ELY} and an electricity-consumption coefficient c^{COM} (MWh/kg) [20]:

$$c^{COM} = \left(\frac{10^{-6}}{3600}\right) \cdot \left(\frac{Z_H \cdot K_H \cdot R_g}{MM_H \cdot \eta^{COM}}\right) \cdot \left(\frac{N^{COM} \cdot \gamma}{\gamma - 1}\right) \cdot \left[\left(\frac{b_{out}^{COM}}{b_{in}^{COM}}\right)^{\frac{\gamma-1}{N^{COM}\cdot\gamma}} - 1\right] \quad (10)$$

where Z_H is the H_2 compressibility factor estimated based on b_{in}^{COM} combined with the inlet H_2 temperature K_H (i.e. 300 K assumed here) [21]; R_g is the universal gas constant of 8.314 J/mol-K; terms MM_H and γ denote the molecular mass and specific heat ratio of H_2, which equal 2.15 g/mol and 1.41, respectively; and terms N^{COM} and η^{COM} represent the number of compression stages and the overall compression efficiency, which are assumed here to be 2 [22] and 75% [23], respectively. Based on Equations (4) and (10), the overall power-to-H_2 conversion efficiency $\eta_{P2m,t}^{E+C}$ (kg/MWh) of the HSS can be formulated by:

$$\eta_{P2m,t}^{E+C} = \frac{P_t^{ELY} \cdot \eta_{P2m,t}^{ELY}}{P_t^{ELY} + P_t^{ELY} \cdot \eta_{P2m,t}^{ELY} \cdot c^{COM}} = \frac{\eta_{P2m,t}^{ELY}}{1 + \eta_{P2m,t}^{ELY} \cdot c^{COM}} \quad (11)$$

Table 1 tabulates the key technical parameters of the grid-connected HSS that are selected here for 2030 and 2050 scenarios based on the estimates of the Fuel Cells and Hydrogen 2 Joint Undertaking (FCH2JU) [19] and International Energy Agency (IEA) [1, 24]. It is noted that the HSS components are assumed here to be always in either working or hot standby mode due to the response-speed requirement of frequency-response services, though their hot standby consumptions accounting for a small part of total electricity export/import are not formulated in Equation (1) for brevity.

1.2 Dynamic regulation frequency response

1.2.1 *Technical requirements*

Dynamic regulation (DR) is one of the three end-state frequency-response products in Great Britain that is procured by the National Grid Electricity System Operator (NGESO) in 4-hourly electricity forward agreement (EFA) blocks to slowly correct continuous but small grid frequency deviations from the nominal level of 50 Hz [26]. Compared with the other two products, i.e. dynamic containment [27] and dynamic moderation [28], which require a response time of 1 second, the maximum response time of the DR service is 10 seconds [26], which can be met by electrolysers and fuel cells given their ramping capability as specified in Table 1. Furthermore, a DR provider is allowed to provide low-frequency (LF) and high-frequency (HF) services separately with unequal capacities (represented by $\overline{P}_{LF}^{DR}$ and $\overline{P}_{HF}^{DR}$, respectively) between 1 and 50 MW [26]. This means that an HSS-based provider can optimize the combination of $\overline{P}_{LF}^{DR}$ and $\overline{P}_{HF}^{DR}$ (which are mainly provided by the fuel cell and the electrolyser, respectively) based on a variety of techno-economic elements including DR delivery performance/payments, HSS costs and efficiencies. A typical frequency-response curve followed by a DR provider as a percentage of its contracted DR capacities and the frequency-response curves for three different combinations of $\overline{P}_{LF}^{DR}$ and $\overline{P}_{HF}^{DR}$ are shown in Fig. 2a and b, respectively. In addition, an energy-limited DR provider like the HSS must be able to sustain full-capacity responses for ≥1 hour in each direction [26], which specifies a minimum energy requirement (MER) for the DR market participants.

1.2.2 *Operational baselines and state of energy rules*

A DR provider needs to report its operational baseline (OB) that will be followed over a future half-hour settlement period (SP) prior to the gate closure of that SP (i.e. at least 1 hour before the

Table 1: Key technical parameters of the grid-connected HSS selected for 2030 and 2050 scenarios

Technical parameters		Symbol	Unit	2030	2050	Reference
PEM electrolyser	Power capacity	$\overline{P}^{ELY}$	MW	To be optimized		–
	Power-to-H_2 efficiency[a]	$\overline{\eta}_{P2m}^{ELY}$	kg of H_2/MWh	20.4	22.2	[24]
	H_2O-to-H_2 efficiency[a]	$\overline{\eta}_{v2m}^{ELY}$	kg of H_2/m³ of H_2O	75.6	82.2	[24]
	Outlet pressure	b_{out}^{ELY}	bar	60	80	[24]
	Lifetime	T_{Life}^{ELY}	Operating hours	90 000	120 000	[24]
	Ramp up/down rate	n/a	% of nominal load/s	100		[19]
	Load range	n/a	% of nominal load	0–160		[19]
Storage tank	Storage capacity	$\overline{M}^{STR}$	kg	To be optimized		–
	Storage pressure	b_{in}^{STR}	bar	350		[19]
Compressor	H_2 flow capacity	$\overline{m}^{COM}$	kg of H_2/h	$\overline{P}^{ELY} \cdot \overline{\eta}_{P2m}^{ELY}$		–
	Compression stage	N^{COM}	n/a	2		[22]
	Inlet pressure[c]	b_{in}^{COM}	bar	b_{out}^{ELY}		–
	Outlet pressure[c]	b_{out}^{COM}	bar	b_{in}^{STR}		–
	Compression efficiency	η^{COM}	–	75%		[23]
Fuel cell	Power capacity	$\overline{P}^{FCL}$	MW	To be optimized		–
	H_2-to-power efficiency[b]	$\overline{\eta}_{m2P}^{FCL}$	MWh/kg of H_2	1/55.56	1/52.63	[1]
	H_2-to-H_2O efficiency[b]	$\overline{\eta}_{m2v}^{FCL}$	m³ of H_2O/kg of H_2	1/205.76	1/194.93	[1]
	Lifetime	T_{Life}^{FCL}	Operating hours	80 000		[1]
	Ramp up/down rate	n/a	% of nominal power/s	10		[19]
	Power range	n/a	% of nominal power	0–100		[19]
Converter	Power capacity	$\overline{P}^{CON}$	MW	$\overline{P}^{ELY}$ or $\overline{P}^{FCL}$- based		–
	AC-to-DC efficiency	η_{A2D}^{CON}	–	95%		[25]
	DC-to-AC efficiency	η_{D2A}^{CON}	–	95%		[25]

[a]The power-to-H_2 and H_2O-to-H_2 efficiencies of the electrolyser are converted from the percentage efficiency of 68% for 2030 or 74% for 2050.
[b]The H_2-to-power and H_2-to-H_2O efficiencies of the fuel cell are converted from the percentage efficiency of 54% for 2030 or 57% for 2050 based on that 30 kg of H_2 contains 1 MWh of usable energy and 1 m³ of H_2O contains 111.1 kg of H_2.
[c]The inlet or outlet pressure of the compressor is presumed to be equal the outlet pressure of the electrolyser or the pressure level of the storage tank, respectively.

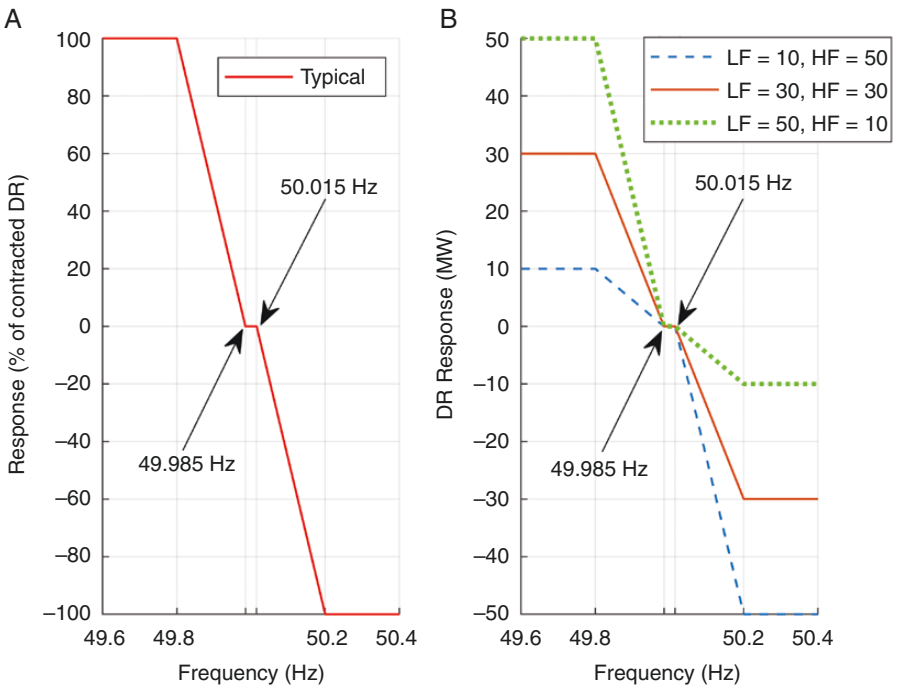

Fig. 2: (a) A typical DR response curve (% of contracted capacities) and (b) DR curves (MW) for different combinations of contacted LF and HF capacities.

SP). This allows an HSS-based provider to manage its H_2 storage level by submitting and following OBs in half-hour SPs at the same time as the delivery of DR services. This also means that the power output of a DR provider will be the sum of its OB and DR response.

To encourage the participation of energy-limited assets, the NGESO has particularly designed the state of energy (SOE) rules that indicate in which cases an energy-limited asset will not be penalized for the under-delivery of DR. To comply with the rules throughout a contracted EFA block, the asset must start the EFA block with an initial energy footroom or headroom level meeting the MER for LF or HF DR, respectively, and then restore ≥20% of the MER in a single SP through its OB subject to the deviation from the MER. In addition, the OB must meet the maximum ramp-rate requirement, which is 5% of the contracted DR capacity per minute [29]. Even though obeying the SOE rules can avoid under-delivery penalties, it requires equipping the energy-limited asset with a sufficient storage capacity to encounter the unpredictable response needs and also with a sufficient headroom in power capacity (i.e. the rise above its contracted DR capacity) for the storage restoration via OBs, which will largely increase the asset investments. The trade-off between following the SOE rules and increasing the asset investments will be addressed here by the optimization method.

1.3 OB submission

Driven by the concept of the SOE rules, a pair of H_2 storage-related variables comprising the target storage footroom M_{ft}^{STR} and headroom M_{hd}^{STR} are introduced here to regulate the OB submission for the H_2 storage restoration. Since the OB submitted by the end of the SP i will take effect across the time steps (t = 1,…,T) within the 1-hour-ahead SP (i + 3), the H_2 storage $M_{i+2,T}^{STR}$, at the end of the SP (i + 2) is first predicted based on the present storage level $M_{i,t-1}^{STR}$ combined with the constant OBs P_i^{OB}, P_{i+1}^{OB} and P_{i+2}^{OB} that have been submitted for SPs i, (i + 1) and (i + 2), respectively. The calculation steps for $M_{i+2,T}^{STR}$ are formulated by Equation (12):

$$\begin{cases} M_{i,T}^{STR} = \begin{cases} \max\left(\mathbb{N}\left\{M_{i,t-1}^{STR} - P_i^{OB}/\left(\eta_{D2A}^{CON}\cdot\eta_{m2P,i,t}^{FCL}\right)\cdot\right.\right. \\ \left.\left.(T-(t-1))\cdot\Delta t\right\},\ \overline{M}^{STR}\right), & \forall P_i^{OB}\geq 0 \\ \max\left(\mathbb{N}\left\{M_{i,t-1}^{STR} - P_i^{OB}\cdot\eta_{A2D}^{CON}\cdot\eta_{P2m,i,t}^{E+C}\cdot\right.\right. \\ \left.\left.(T-(t-1))\cdot\Delta t\right\},\ \overline{M}^{STR}\right), & \forall P_i^{OB}<0 \end{cases} \\ M_{i+1,T}^{STR} = \begin{cases} \max\left(\mathbb{N}\left\{M_{i,T}^{STR} - P_{i+1}^{OB}/\left(\eta_{D2A}^{CON}\cdot\eta_{m2P,i,t}^{FCL}\right)\cdot\right.\right. \\ \left.\left.0.5\ h\right\},\ \overline{M}^{STR}\right), & \forall P_{i+1}^{OB}\geq 0 \\ \max\left(\mathbb{N}\left\{M_{i,T}^{STR} - P_{i+1}^{OB}\cdot\eta_{A2D}^{CON}\cdot\eta_{P2m,i,t}^{E+C}\cdot\right.\right. \\ \left.\left.0.5\ h\right\},\ \overline{M}^{STR}\right), & \forall P_{i+1}^{OB}<0 \end{cases} \\ M_{i+2,T}^{STR} = \begin{cases} \max\left(\mathbb{N}\left\{M_{i+1,T}^{STR} - P_{i+2}^{OB}/\left(\eta_{D2A}^{CON}\cdot\eta_{m2P,i,t}^{FCL}\right)\cdot\right.\right. \\ \left.\left.0.5\ h\right\},\ \overline{M}^{STR}\right), & \forall P_{i+2}^{OB}\geq 0 \\ \max\left(\mathbb{N}\left\{M_{i+1,T}^{STR} - P_{i+2}^{OB}\cdot\eta_{A2D}^{CON}\cdot\eta_{P2m,i,t}^{E+C}\cdot\right.\right. \\ \left.\left.0.5\ h\right\},\ \overline{M}^{STR}\right), & \forall P_{i+2}^{OB}<0 \end{cases} \end{cases} \quad (12)$$

where the term (T – (t – 1)) is the number of remaining time steps in the present SP i. Then the total H_2 mass M_{gap}^{STR} required to replenish or release for restoration to M_{ft}^{STR} or M_{hd}^{STR} prior to the subsequent EFA block is estimated by Equation (13):

$$M_{gap}^{STR} = \begin{cases} M_{i+2,T}^{STR} - M_{ft}^{STR}, & \forall M_{i+2,T}^{STR} < M_{ft}^{STR} \\ 0, & \forall M_{ft}^{STR} \leq M_{i+2,T}^{STR} \leq \left(\overline{M}^{STR} - M_{hd}^{STR}\right) \\ M_{i+2,T}^{STR} - \left(\overline{M}^{STR} - M_{hd}^{STR}\right), & \forall M_{i+2,T}^{STR} > \left(\overline{M}^{STR} - M_{hd}^{STR}\right) \end{cases} \quad (13)$$

Finally, when it comes to the end of the SP i, the magnitude of the OB P_{i+3}^{OB} submitted for the SP (i + 3) must be limited to the rise of the HSS's total power-import capacity (i.e. $\overline{P}^{ELY}\cdot\left(1+\eta_{P2m,i,t}^{ELY}\cdot e^{COM}\right)/\eta_{A2D}^{CON}$) above $\overline{P}_{HF}^{DR}$ or the rise of the HSS's power-export capacity (i.e. $\overline{P}^{FCL}\cdot\eta_{D2A}^{CON}$) above $\overline{P}_{LF}^{DR}$, so as to ensure that the HSS can deliver full DR responses at the same time as following OBs. Furthermore, the OB P_{i+3}^{OB} is specifically determined to restore the H_2 storage by the median of (i) M_{gap}^{STR}, (ii) average H_2 mass (i.e. M_{gap}^{STR}/N) distributed across N SPs from the SP (i + 3) to

the start of its subsequent EFA block and (iii) the H_2 mass equivalent to 20% of the MER as required by the SOE rules. This not only helps meet the energy-storage restoration requirement in the rules but also reduces the OB magnitudes, avoiding the need for an excessive headroom in the HSS power capacity for H_2 restoration.

1.4 DR delivery and operating strategy

Two different system configurations are particularly designed here for a wind-farm owner to co-locate an onshore HSS for the DR provision, as shown in Figs 3 and 4. The HSS delivers DR responses to the main AC grid via the common connection point only in a non-power-exchange (NPE) configuration (see Fig. 3), whereas an additional converter is placed in a power-exchange (PE) configuration (see Fig. 4) to enable the energy interchange between the wind farm and the HSS at the same time as the DR provision. The energy exchange of the co-location system with the main AC grid is monitored by the wind-farm meter and HSS meter, respectively, for the estimation of related revenue streams or charges, though the energy interchange across the behind-the-meter additional converter within the co-location system itself does not contribute to economic calculations. It is noted that the wind farm and HSS cannot interchange energy through the path crossing the two meters, which would otherwise interfere with the monitoring on the system export to or import from the main AC grid and related economics. The AC–DC conversion efficiencies of the additional converter (denoted by η_{A2D}^{AdC} and η_{D2A}^{AdC}) are assumed to equal those of the HSS converter (see Table 1). This section details the DR delivery of the HSS and the coordination of the co-location system in each configuration.

1.4.1 *NPE configuration*

DR delivery in NPE.

The aggregate power output $P_{i,t}^{DC}$ of the HSS is driven by the sum of the OB P_i^{OB} and the DR response requirement $P_{Req,i,t}^{DR}$ determined from the DR curve (see Fig. 2) subject to the available H_2 storage footroom or headroom in the storage tank, as formulated by Equation (14) with $P_{Req,i,t}^{B+R} = \left(P_i^{OB} + P_{Req,i,t}^{DR}\right)$. Then the resulting $P_{i,t}^{DC}$ is split between $P_{i,t}^{ELY}$ and $P_{i,t}^{COM}$ when $P_{i,t}^{DC} < 0$ or attributed to $P_{i,t}^{FCL}$ for $P_{i,t}^{DC} > 0$, based on which $M_{i,t}^{STR}$ and $v_{i,t}^{EXT}$ are updated by using Equations (2–5). When the storage tank has an insufficient H_2 storage footroom or headroom, the under-delivery of the LF or HF DR is quantified by a percentage error, denoted by $\varepsilon_{i,t}^{LF}$ or $\varepsilon_{i,t}^{HF}$, using Equation (15) or (16), respectively:

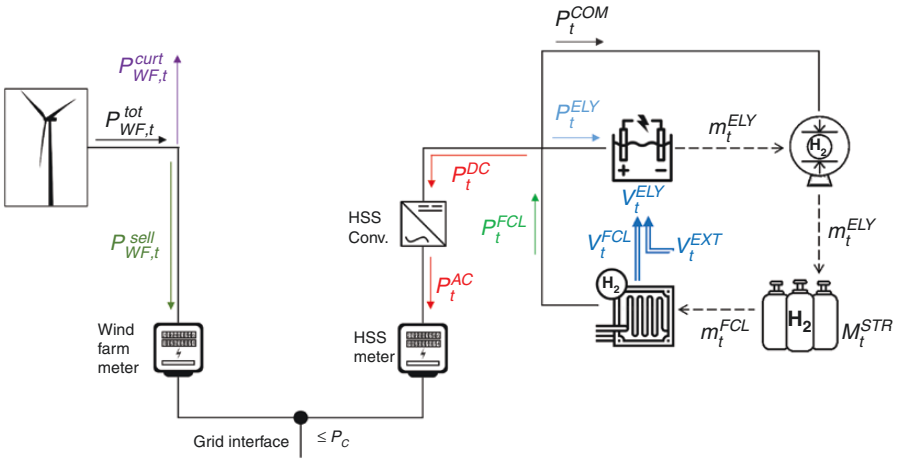

Fig. 3: The non-power-exchange configuration for a wind-farm and HSS co-location system.

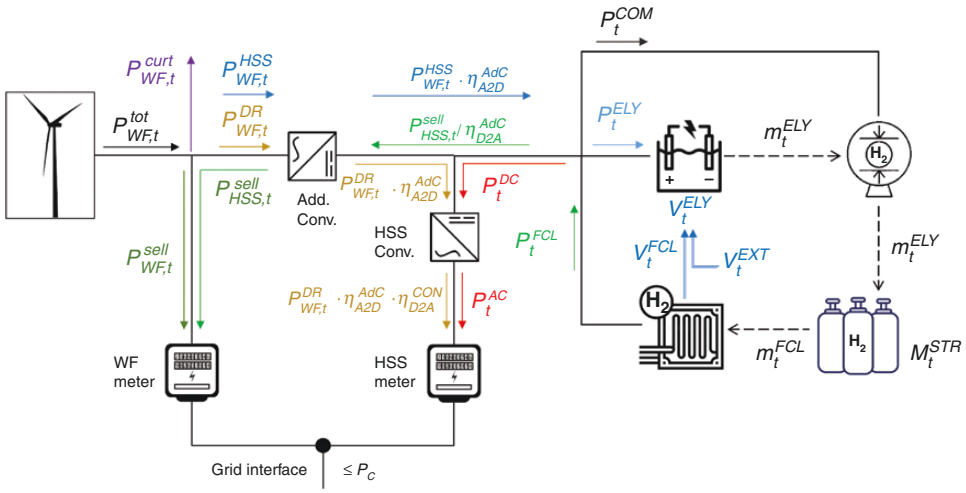

Fig. 4: The power-exchange configuration for a wind-farm and HSS co-location system.

$$P_{i,t}^{DC}=\begin{cases}\min\left(P_{Req,i,t}^{B+R}/\eta_{D2A}^{CON},\ \frac{M_{i,t-1}^{STR}\cdot\eta_{m2P,i,t}^{FCL}}{\Delta t}\right), & \forall P_{Req,i,t}^{B+R}\geq 0\\ \max\left(P_{Req,i,t}^{B+R}\cdot\eta_{A2D}^{CON},\ \frac{M_{i,t-1}^{STR}-\overline{M}^{STR}}{\eta_{P2m,i,t}^{E+C}\cdot\Delta t}\right), & \forall P_{Req,i,t}^{B+R}<0\end{cases} \quad (14)$$

$$\varepsilon_{i,t}^{LF}=\begin{cases}\left|P_{i,t}^{AC}-P_{Req,i,t}^{B+R}\right|/\overline{P}_{LF}^{DR}, & \forall P_{Req,i,t}^{DR}>0\\ 0, & \forall P_{Req,i,t}^{DR}\leq 0\end{cases} \quad (15)$$

$$\varepsilon_{i,t}^{HF}=\begin{cases}0, & \forall P_{Req,i,t}^{DR}\geq 0\\ \left|P_{i,t}^{AC}-P_{Req,i,t}^{B+R}\right|/\overline{P}_{HF}^{DR}, & \forall P_{Req,i,t}^{DR}<0\end{cases} \quad (16)$$

Wind farm–HSS coordination in NPE.

Due to the limited ampacity P_C of the common connection point, the HSS exporting to the main grid (i.e. $P_{i,t}^{AC}>0$) will reduce the connection ampacity headroom available for wind-farm outputs, which may cause wind curtailments especially in high-wind periods. In this study, the power flow across the wind-farm meter is assumed to be constrained by P_C only. In order to avoid that some part of the HF response (i.e. $P_{Req,i,i}^{DR}<0$) or the OB for energy import (i.e. $P_i^{OB}<0$) unexpectedly comes from any exceedance of the available wind power $P_{WF,i,t}^{tot}$ beyond the limit of P_C, i.e. the wind power to be curtailed, the power flow across the wind-farm meter $P_{WF,i,t}^{sell}$ is additionally limited by P_C, as formulated by Equation (17):

$$P_{WF,i,t}^{sell}=\min\left(P_{WF,i,t}^{tot},\ \left(P_C-\mathbb{N}\left\{P_{i,t}^{AC}\right\}\right)\right) \quad (17)$$

1.4.2 PE configuration

DR delivery in PE.

Another pair of H_2 storage-related variables, denoted by M_{ch}^{STR} and M_{dis}^{STR}, are introduced for the PE configuration to guide the power interchange between the HSS and the wind farm across the additional converter. Furthermore, the deployment of the additional converter allows the wind farm to assist the HSS in the power export to the main AC grid when there is wind curtailment and/or an insufficient H_2 storage for the required export. When the HSS is required to import electricity from the main AC grid, i.e. $P_{Req,i,t}^{B+R}<0$, the power $P_{i,t}^{DC}$ that can be absorbed by the HSS (or electrolyser and compressor in this case) and resulting response error $\varepsilon_{i,t}^{LF}$ or $\varepsilon_{i,t}^{HF}$ are computed in the same way as Equations (14–16). For $P_{Req,i,t}^{B+R}\geq 0$, the otherwise curtailed wind power (if any) is first considered to assist the HSS in the delivery of $P_{Req,i,t}^{B+R}$ through transferring across the additional converter to the HSS meter by $P'^{HSS}_{WF,i,t}$ subject to the power capacity $\overline{P}^{AdC}$ of the additional converter:

$$P'^{HSS}_{WF,i,t}=\min\left(\mathbb{N}\left\{P_{WF,i,t}^{tot}-\left(P_C-P_{Req,i,t}^{B+R}\right)\right\},\ \overline{P}^{AdC},\ \frac{1}{\eta_{A2D}^{AdC}}\cdot\mathbb{N}\left\{\frac{P_{Req,i,t}^{B+R}}{\eta_{D2A}^{CON}}-\mathbb{N}\left\{\frac{\left(M_{i,t-1}^{STR}-M_{ch}^{STR}\right)}{\Delta t/\eta_{m2P,i,t}^{FCL}}\right\}\right\}\right),\quad \forall P_{Req,i,t}^{B+R}\geq 0 \quad (18)$$

where the power equivalent to any rise in the present storage $M_{i,t-1}^{STR}$ above M_{ch}^{STR} is subtracted from the required $P_{Req,i,t}^{B+R}$ in order to avoid the transfer of otherwise curtailed wind power to the HSS meter mitigating the fuel-cell export and resulting in an excessive H_2 storage level (i.e. little H_2 storage headroom). Then if the HSS still has insufficient H_2 storage to deliver the required export after the transfer of $P'^{HSS}_{WF,i,t}$, the wind farm is regulated here to assist the HSS further in filling the export shortage subject to the remaining wind power and the remaining ampacity of the additional converter. This is formulated by Equation (19), which estimates the total wind-power flow $P_{WF.i,t}^{HSS}$ that will transfer across the additional converter to the HSS meter. Finally, the power export $P_{t,i}^{DC}\geq 0$ from the HSS (or fuel cell in this case) to the HSS meter, together with the resulting response error $\varepsilon_{i,t}^{LF}$ or $\varepsilon_{i,t}^{HF}$, is calculated based on Equations (14–16) by subtracting $\left(P_{WF,i,t}^{HSS}\cdot\eta_{A2D}^{AdC}\cdot\eta_{D2A}^{CON}\right)$ from the required $P_{Req,i,t}^{B+R}$:

$$P_{WF,i,t}^{HSS}=P'^{HSS}_{WF,i,t}+\min\left(\left(P_{WF,i,t}^{tot}-P'^{HSS}_{WF,i,t}\right),\ \left(\overline{P}^{AdC}-P'^{HSS}_{WF,i,t}\right),\ \frac{1}{\eta_{A2D}^{AdC}}\cdot\mathbb{N}\left\{\frac{P_{Req,i,t}^{B+R}}{\eta_{D2A}^{CON}}-P'^{HSS}_{WF,i,t}\cdot\eta_{A2D}^{AdC}-\frac{M_{i,t-1}^{STR}\cdot\eta_{m2P,i,t}^{FCL}}{\Delta t}\right\}\right),\quad \forall P_{Req,i,t}^{B+R}\geq 0 \quad (19)$$

Wind farm–HSS coordination in PE.

Based on the estimated power transfers of $P_{t,i}^{DC}$ and $P_{WF,i,t}^{HSS}$ across the HSS meter, the wind power $P_{WF,i,t}^{sell}$ sold to the main AC grid across the wind-farm meter is estimated by Equation (20) subject to the connection ampacity:

$$P_{WF,i,t}^{sell}=\min\left(\left(P_{WF,i,t}^{tot}-P_{WF,i,t}^{HSS}\right),\ \left(P_C-\mathbb{N}\left\{P_{i,t}^{AC}+P_{WF,i,t}^{HSS}\cdot\eta_{A2D}^{AdC}\cdot\eta_{D2A}^{CON}\right\}\right)\right) \quad (20)$$

When the available wind power $P_{WF,i,t}^{tot}$ exceeds $\left(P_{WF,i,t}^{sell}+P_{WF,i,t}^{HSS}\right)$, some part of the otherwise curtailed wind power can be absorbed by the HSS (denoted by $P_{WF,i,t}^{E+C}$) subject to the remaining capacities of the electrolyser and additional converter as well as the present headroom in the storage tank and the rise in M_{ch}^{STR} above the H_2 storage prediction $M_{i+2,T}^{STR}$:

$$P_{WF,i,t}^{E+C}=\min\begin{pmatrix}\left(P_{WF,i,t}^{tot}-P_{WF,i,t}^{sell}-P_{WF,i,t}^{HSS}\right),\\ \left(\overline{P}^{ELY}\cdot\left(1+\eta_{P2m,i,t}^{ELY}\cdot c^{COM}\right)\right.\\ \left.-\mathbb{N}\left\{-P_{i,t}^{DC}\right\}\right)/\eta_{A2D}^{AdC},\\ \left(\overline{P}^{AdC}-P_{WF,i,t}^{HSS}\right),\\ \left(\frac{\overline{M}^{STR}-M'^{STR}_{i,t}}{\eta_{P2m,i,t}^{E+C}\cdot\eta_{A2D}^{AdC}\cdot\Delta t}\right),\quad \mathbb{N}\left\{\frac{M_{ch}^{STR}-M_{i+2,T}^{STR}}{\eta_{P2m,i,t}^{E+C}\cdot\eta_{A2D}^{AdC}\cdot\Delta t}\right\}\end{pmatrix} \quad (21)$$

where the term $M'^{STR}_{i,t}$ is the H_2 storage level if the HSS would deliver $P_{t,i}^{DC}$ only over Δt.

When there is still a headroom in the connection ampacity, the fuel cell is considered to consume H_2 and export to the wind-farm meter via the additional converter subject to the available capacities of additional converter and fuel cell as well as the present H_2 storage and the rise in the storage prediction $M_{i+2,T}^{STR}$ above M_{dis}^{STR}. To avoid any flow to the main AC grid via the wind-farm meter coming unexpectedly from the HF response (i.e. $P_{Req,i,t}^{DR}<0$) or the OB for energy import (i.e. $P_i^{OB}<0$), the HSS export to the main AC grid via the wind-farm meter (denoted by $P_{HSS,i,t}^{sell}$) is constrained to zero in these cases. When $P_{Req,i,t}^{DR}$ and P_i^{OB} are both non-negative, the export $P_{HSS,i,t}^{sell}$ is formulated by Equation (22):

$$P_{HSS,i,t}^{sell}=\min\begin{pmatrix}\left(P_C-P_{WF,i,t}^{sell}-\mathbb{N}\left\{P_{WF,i,t}^{HSS}\cdot\eta_{A2D}^{AdC}\cdot\eta_{D2A}^{CON}+P_{i,t}^{AC}\right\}\right),\\ \left(\overline{P}^{FCL}-\mathbb{N}\left\{P_{i,t}^{DC}\right\}\right)\cdot\eta_{D2A}^{AdC},\\ \left(\overline{P}^{AdC}+P_{WF,i,t}^{HSS}\right),\\ \left(\frac{M'^{STR}_{i,t}\cdot\eta_{m2P,i,t}^{FCL}}{\Delta t/\eta_{D2A}^{AdC}}\right),\quad \frac{\mathbb{N}\left\{M_{i+2,T}^{STR}-M_{dis}^{STR}\right\}}{\Delta t/\left(\eta_{D2A}^{AdC}\cdot\eta_{m2P,i,t}^{FCL}\right)}\end{pmatrix},\quad \forall P_{Req,i,t}^{DR}\geq 0\cap P_i^{OB}\geq 0 \quad (22)$$

Finally, the power flow of the HSS across the HSS meter (i.e. $P_{i,t}^{AC}$) together with its power interchange with the wind farm (i.e. $P_{WF,i,t}^{E+C}$ and $P_{HSS,i,t}^{sell}$) are translated into the eventual power import/export of the electrolyser, compressor and fuel cell, based on which the H_2 storage $M_{i,t}^{STR}$ and the external freshwater import $v_{i,t}^{EXT}$ at the end of time step t are updated by Equations (2–5).

2 Techno-economic optimization

This section describes the application of the PSO method to the techno-economic optimization of the wind-farm and HSS co-location system. The PSO problem is formulated here by comparing revenue streams and costs between the co-location system and a stand-alone wind farm without the HSS connection. The DR service payments, HSS costs, additional revenue (or losses) and connection charges of the co-location system due to the HSS operation are detailed in this section. It is noted that the HSS sharing the connection point of the wind farm can avoid the significant costs of new infrastructure or reinforcement that would otherwise be required by an offsite HSS connection, though the HSS export across the common connection point might cause wind curtailment and associated revenue losses in high-wind periods.

2.1 DR availability payment

Although a DR provider might link its LF tenders with HF tenders in the DR service auctions, the DR availability payments are evaluated here for LF and HF services separately. As was noted in Section 1.2.2, the HSS complying with the SOE rules can receive a full DR availability payment for the contracted EFA block e. However, when the SOE rules are not fulfilled in the block e, the maximum percentage error of LF or HF responses monitored in the block will be translated into a performance factor (K_e^{LF} or K_e^{HF}) by Equation (23), which is then used to estimate the LF or HF DR payment (R_e^{LF} or R_e^{HF}) for that EFA block by Equation (24) [26] (the calculation of the LF DR payment is presented here only for brevity):

$$K_e^{LF} = \mathbb{N}\left\{1 - \mathbb{N}\left\{\frac{\max\left(\varepsilon_{e,i,t}^{LF}\right) - 5\%}{25\% - 5\%}\right\}\right\} \tag{23}$$

$$R_e^{LF} = \mathcal{P}^{LF} \cdot \overline{P}_{LF}^{DR} \cdot K_e^{LF} \cdot \sum_i \left(A_{e,i}^{LF} \cdot 0.5\ \text{h}\right) \tag{24}$$

where the term $A_{e,i}^{LF}$ equals 1 if the required LF responses are delivered throughout the half-hour SP i within the EFA block e; otherwise, $A_{e,i}^{LF} = 0$. The DR unit price $\mathcal{P}^{LF}$ is presumed here to be £20/MWh, though the minimum possible DR tendered prices for a profitable HSS co-location project will be estimated from the optimization-based cost–benefit analysis in Section 3.4.

2.2 HSS economics

The key economic parameters employed here to evaluate the capital expenditure (CAPEX) and operating expenses (OPEX) of different HSS components in 2030 and 2050 scenarios are listed in Table 2 mainly based on FCH2JU [19] and IEA [1, 24]. It is noted that the economics estimated by the references for past years or different currency units have been converted to 2019 values in GBP (British pound sterling). Except for the compressor, the CAPEX and OPEX of other HSS components are assumed here to be linearly dependent on their capacities. The CAPEX of the compressor C_{CAP}^{COM} is approximately estimated here by Equation (25) based on the system CAPEX C_{CAP}^{COMr} of a reference compressor that has a nominal flow rate $\overline{m}^{COMr}$ of 50 kg/h with inlet pressure b_{in}^{COMr} and outlet pressure b_{out}^{COMr} of 30 and 200 bar, respectively [19]. Then the annual OPEX C_{OP}^{COM} of the compressor is assumed to be 4% of its CAPEX.

$$C_{CAP}^{COM} = C_{CAP}^{COMr} \cdot \left(\frac{\overline{m}^{COM}}{\overline{m}^{COMr}}\right)^{0.66} \cdot \left(\frac{b_{out}^{COM}/b_{in}^{COM}}{b_{out}^{COMr}/b_{in}^{COMr}}\right)^{0.25} \cdot \left(\frac{b_{out}^{COM}}{b_{out}^{COMr}}\right)^{0.25} \tag{25}$$

2.3 Additional revenue (loss) and connection charge

2.3.1 *Operational baseline-related*

The electricity export and import of the HSS through its OBs require contracting with suppliers and generators, respectively, in electricity markets. Although these contracts would be generally made within the day, the day-ahead electricity prices in the UK [31] are employed here to approximate the private-contract prices $\mathcal{P}_i^{OB}$ (£/MWh) and estimate the OB-related revenue or cost R_e^{OB} in the EFA block e:

$$R_e^{OB} = \sum_i \mathcal{P}_i^{OB} \cdot P_i^{OB} \cdot 0.5\ \text{h} \tag{26}$$

2.3.2 *Green subsidy*

As was noted in Section 1.4, the power export of the co-located HSS will compress the headroom in the connection ampacity

Table 2: Key economic parameters of the grid-connected HSS selected for 2030 and 2050 scenarios

Techno-economic parameter		Symbol	Unit	2030	2050	Reference
PEM electrolyser	Unit CAPEX	$\mathcal{P}_{CAP}^{ELY}$	£/MW of electrolyser	602.17k	481.77k	[24]
	Unit annual OPEX	$\mathcal{P}_{OP}^{ELY}$	£/MW of electrolyser/yr	12.04k	9.64k	[19]
	Unit replacement cost	$\mathcal{P}_{REP}^{ELY}$	£/MW of electrolyser	180.65k	144.53k	[19]
	Water unit price	$\mathcal{P}_{H2O}^{EXT}$	£/m³ of H2O	3.56		[19]
Storage tank	Unit CAPEX	$\mathcal{P}_{CAP}^{STR}$	£/kg of H_2	440.8		[19]
	Unit annual OPEX	$\mathcal{P}_{OP}^{STR}$	£/kg of H_2/yr	8.82		[19]
Compressor	Reference capacity	$\overline{m}^{COMr}$	kg of H_2/h	50		[19]
	Reference inlet pressure	b_{in}^{COMr}	bar	30		[19]
	Reference outlet pressure	b_{out}^{COMr}	bar	200		[19]
	Reference CAPEX	C_{CAP}^{COMr}	£	281.39k		[19]
	Reference annual OPEX	C_{OP}^{COMr}	£/yr	5.63k		[19]
Fuel cell	Unit CAPEX	$\mathcal{P}_{CAP}^{FCL}$	£/MW of fuel cell	624.75k	496.79k	[1]
	Unit annual OPEX	$\mathcal{P}_{OP}^{FCL}$	£/MW of fuel cell/yr	31.24k	24.84	[1]
	Unit replacement cost	$\mathcal{P}_{REP}^{FCL}$	£/MW of fuel cell	312.38k	248.40k	[19]
Converter	Unit CAPEX	$\mathcal{P}_{CAP}^{CON}$	£/MW of converter	75k		[30]
	Unit annual OPEX	$\mathcal{P}_{OP}^{CON}$	£/MW of converter/yr	1.5k		[30]

and might cause the curtailment of wind generation that would otherwise be delivered to the main grid. Compared with a single wind farm whose wind export to the main grid is presumed to be the minimum of $P^{tot}_{WF,i,t}$ or P_C, the additional wind curtailment induced by the HSS co-location will reduce the green subsidy received by the wind farm. The contracts for difference (CFD) scheme is the main green-subsidy mechanism in the UK that pays accredited renewable generators for their export to the main grid at a price $\mathcal{P}^{CFD}$ (£/MWh) equalling the difference between a technology-dependent 'strike price' and an electricity-market 'reference price' [32]. Based on the market reference prices and strike prices recorded for offshore wind over 2017–19 [33], their respective averages equalling £48.7/MWh and £165.8/MWh are used here to approximate a CFD price $\mathcal{P}^{CFD}$ of £117.1/MWh and estimate the green-subsidy loss δR^{CFD}_e associated with the wind-export reduction:

$$\delta R^{CFD}_e = \sum_i \sum_t \mathcal{P}^{CFD} \cdot \left(P^{sell}_{WF,i,t} - \min\left(P^{tot}_{WF,i,t},\ P_C\right)\right) \cdot \Delta t \tag{27}$$

2.3.3 Energy-imbalance charge

When the actual outputs of the wind farm and the HSS to the main grid deviate from their contracted electricity volumes in the SP i, they will pay (or be paid) for the net deficit (or surplus) of energy imbalance at an imbalance price $\mathcal{P}^{EIC}_i$ (£/MWh) that reflects the cost of the NGESO balancing the transmission system in that SP [34]. Compared with a single wind farm, the energy-imbalance charge (EIC) variation δR^{EIC}_e after the HSS co-location is estimated by Equation (28) based on the difference in power flow across the wind-farm meter between a single wind farm and the co-location system in combination with the deviation of power flow across the HSS meter from the OB:

$$\begin{aligned}\delta R^{EIC}_e = \sum_i \sum_t \mathcal{P}^{EIC}_i \cdot \Big(&\left(P^{sell}_{WF,i,t} + P^{sell}_{HSS,i,t}\right) - \\ &\min\left(P^{tot}_{WF,i,t},\ P_C\right) + \\ &\left(P^{HSS}_{WF,i,t} \cdot \eta^{AdC}_{A2D} \cdot \eta^{CON}_{D2A} + P^{AC}_{i,t} - P^{OB}_i\right)\Big) \cdot \Delta t\end{aligned} \tag{28}$$

2.3.4 Connection charge

Given the wind farm having an existing connection point between 100 and 1320 MW, the application for the connection point modification for the HSS co-location without varying its connection ampacity will induce a charge C_{APP} of ~£105.2k based on the median base cost of the six connection zones in Great Britain [35]. The operation of the co-located HSS will also influence the transmission network use of system (TNUoS) and balancing services use of system (BSUoS) charges that are paid by generators and suppliers for using the transmission system for electricity delivery [36] and for the costs of balancing service activities taken by the NGESO [37], respectively. The TNUoS charges paid by a power plant depend on its (predominant) fuel type and annual load factor. Given the use of a generic annual load factor estimate of 10.8% for energy storage prior to any historic data being available, the annual TNUoS growth δC^{TN}_{ann} of the wind farm caused by the HSS co-location is evaluated to be the product of £919.6/MW and the AC capacity of the fuel cell $\left(\overline{P}^{FCL} \cdot \eta^{CON}_{D2A}\right)$ based on the TNUoS tariffs specified for a particular zone in 2019/2020 [38]. The BSUoS charge variation δC^{BS}_e after the HSS co-location is estimated based on the deviation of power flow across the connection point from a single wind farm in combination with the BSUoS unit price $\mathcal{P}^{BS}_i$ (£/MWh) assigned to each SP [39]:

$$\begin{aligned}\delta C^{BS}_e = \sum_i \sum_t \mathcal{P}^{BS}_i \cdot \Big(&\left|P^{sell}_{WF,i,t} + P^{sell}_{HSS,i,t} + P^{HSS}_{WF,i,t} \cdot \eta^{AdC}_{A2D} \cdot \eta^{CON}_{D2A} + P^{AC}_{i,t}\right| - \\ &\min\left(P^{tot}_{WF,i,t},\ P_C\right)\Big) \cdot \Delta t\end{aligned} \tag{29}$$

2.4 Implementation of PSO

The planning of the co-location system, including the optimal HSS component capacities, contracted capacities of LF and HF DR, and H_2 storage-related strategy variables, are optimized here from the perspective of an economic optimization subject to a set of technical constraints that specify DR market entry requirements. The PSO method [40] is employed here as an optimization tool that forms a particle by a vector of optimization variables, based on which the system operation along with resulting monthly cash flows is simulated to estimate the final NPV at the end of a presumed 15-year project lifespan [25]:

$$\mathrm{NPV} = -C^{HSS}_{CAP} - C_{APP} + \sum_{j=1}^{180} \frac{\sum_e \left(R^{LF}_{j,e} + R^{HF}_{j,e} + R^{OB}_{j,e} + \delta R^{CFD}_{j,e} + \delta R^{EIC}_{j,e} - \delta C^{BS}_{j,e}\right) - \delta C^{TN}_j - C^{HSS}_{OP,j} - C^{HSS}_{REP,j} - C^{EXT}_{H2O,j}}{(1+r)^{j/12}} \tag{30}$$

where j and r represent a month index and an annual return of 8%, respectively; terms C^{HSS}_{CAP} and $C^{HSS}_{OP,j}$ are the overall CAPEX and monthly OPEX of multiple HSS components; terms $C^{HSS}_{REP,j}$ and $C^{EXT}_{H2O,j}$ are the costs of stack replacement and external freshwater import in the month j; and the monthly TNUoS growth δC^{TN}_j is assumed to equal $\delta C^{TN}_{ann}/12$. The NPV of the co-location system estimated for the NPE or PE configuration under the 2030 or 2050 scenario is taken as the objective function and maximized by the PSO method separately subject to:

$$1 \le \overline{P}^{DR}_{LF} \le \min\left(50,\ \overline{P}^{FCL} \cdot \eta^{CON}_{D2A}\right) \tag{31}$$

$$1 \le \overline{P}^{DR}_{HF} \le \min\left(50,\ \overline{P}^{ELY} \cdot \left(1 + \overline{\eta}^{ELY}_{P2m} \cdot c^{COM}\right) / \eta^{CON}_{A2D}\right) \tag{32}$$

$$\left(\overline{P}^{DR}_{LF} \cdot 1\ \ h\right) / \left(\eta^{CON}_{D2A} \cdot \overline{\eta}^{FCL}_{m2P}\right) + \left(\overline{P}^{DR}_{HF} \cdot 1\ \ h\right) \cdot \left(\eta^{CON}_{A2D} \cdot \overline{\eta}^{E+C}_{P2m}\right) \le \overline{M}^{STR} \tag{33}$$

$$M^{STR}_{ft} + M^{STR}_{hd} \le \overline{M}^{STR} \tag{34}$$

$$M^{STR}_{ch} \le \overline{M}^{STR} \tag{35}$$

$$M^{STR}_{dis} \le \overline{M}^{STR} \tag{36}$$

where Equations (31–33) specify the DR market entry requirements including that the contracted capacities of LF and HF DR are met by the power capacity of the fuel cell and the aggregate power capacity of the electrolyser and the compressor, respectively, and that the storage-tank capacity enables the HSS to sustain the full-capacity response for at least 1 hour in each direction. Equations (34–36) additionally force the storage-tank capacity to be greater than or equal to the storage-related strategy variables that guide the OB submission and the power interchange between the wind farm and the HSS, respectively.

3 Optimization results and discussion

The co-location system simulation and the PSO implementation are all accomplished using MATLAB/Simulink [41]. The modelling framework along with the optimization method is tested in the context of a particular 432-MW offshore wind farm in Great Britain with a presumed onshore connection

ampacity of 389 MW (i.e. ~90% of its installed capacity [42]). The available power outputs of the wind farm are estimated based on the virtual wind-farm model developed in [43] that translates the hourly MERRA-2 wind reanalysis data recorded at the location of the wind farm [44] into aggregate wind-farm outputs considering the smoothing effect of 54 8-MW wind turbines across the wind farm. Fig. 5a and b shows the power curve of the wind farm and the resulting hourly available outputs over 4 years from 2016 to 2019, respectively. The 1-second grid frequencies [45], day-ahead electricity prices $\mathcal{P}_i^{OB}$ [31], imbalance prices $\mathcal{P}_i^{EIC}$ [46] and BSUoS prices $\mathcal{P}_i^{BS}$ [39] during the same period are used to estimate the time-varying frequency-response requirements, OB-related revenues or costs, EICs and BSUoS charges, respectively. Due to the difficulty and uncertainty in long-term forecasts of market prices and connection charges, the aforementioned prices over the 4 years prior to the COVID-19 pandemic are employed as an approximation for both 2030 and 2050 scenarios. In other words, the techno-economics of the electrolyser and the fuel cell are the only differences between the 2030 and 2050 scenarios in this work (see Tables 1 and 2), which allows examination of the way in which their techno-economic improvement influences the system optimization. In addition, since the HSS is mainly used here for the DR provision, the power capacities of the electrolyser and the fuel cell would not far exceed the 50-MW cap on the DR tendered capacity. Their power capacities are so small compared with the UK's total generation capacity (i.e. 100 GW above in 2019 [47]) that the co-location of the HSS would have little impact on the electricity-market prices.

This section will first discuss and compare the technical variables of the HSS co-location systems optimized under different configurations and scenarios, followed by detailing the DR delivery performance and operation of the optimized system. Then the optimization-based cost–benefit analysis is implemented to evaluate the profitability of co-locating an HSS for the DR provision and the minimum possible DR tendered prices.

3.1 Co-location system optimization

The optimal technical variables of the co-location systems in NPE and PE configurations under the 2030 and 2050 scenarios are listed in Table 3, respectively. For the system in the NPE configuration, the optimal HF DR capacities reach a maximum of 50 MW under both the 2030 and the 2050 scenarios, with a LF-to-HF capacity ratio equalling ~30% or ~48% under the 2030 or the 2050 scenario, respectively, which is close to the corresponding round-trip efficiency of the HSS (i.e. 33% for 2030 or 38% for 2050). A greater LF-to-HF capacity ratio is suggested under the 2050 scenario due to the reduced costs of the fuel cell and the electrolyser, which incentivize the HSS to use a larger fuel cell for a higher LF capacity combined with a larger electrolyser to increase the maximum allowable magnitude of the OB for H_2 recovery. As indicated by the HSS-converter capacity, which is determined by the aggregate AC power capacity of the electrolyser and compressor, the maximum magnitude of the (importing) OB for H_2 recovery is ~0.2 or ~1.5 MW (i.e. the rise of the HSS-converter capacity above the HF capacity) for 2030 or 2050, respectively.

The optimization of the PE configuration also suggests the provision of 50 MW of HF DR, but with a greater LF DR capacity than the NPE configurations for 2030 and 2050. This is because the employment of the 3- or 5.2-MW additional converter in the PE configuration not only enables the wind farm to assist the HSS in dealing with increased LF responses (i.e. power export across the HSS meter) at times of wind curtailment and/or insufficient H_2 storage, but also allows the HSS to absorb otherwise curtailed wind generation for additional H_2 recovery. Due to the provision of a greater LF capacity in the PE configuration, the maximum OB magnitude for H_2 recovery is increased to ~0.5 MW for 2030 or ~4.8 MW for 2050. However, it is noted that the maximum (exporting) OB magnitude for H_2 release (i.e. the rise in the AC capacity of the fuel cell above the LF capacity) is 0.4 MW only for the NPE under the 2030 scenario or 0 for the other cases, which is in part due to the relatively high investments of fuel cells and in part because the large H_2 consumption for LF responses results

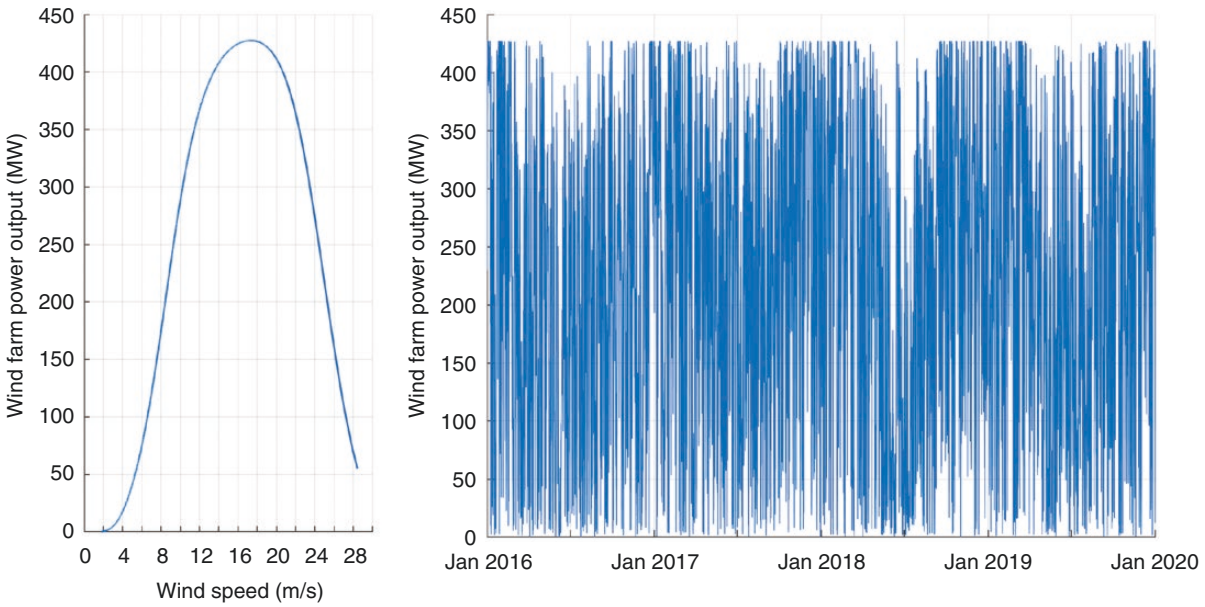

Fig. 5: The power curve and resulting hourly available outputs (MW) of a 432-MW offshore wind farm.

Table 3: Optimization of technical variables of co-location systems in NPE and PE configurations under 2030 and 2050 scenarios

Variable	NPE		PE	
	2030	2050	2030	2050
LF DR capacity (MW)	15.0	24.0	17.0	43.0
HF DR capacity (MW)	50.0	50.0	50.0	50.0
Fuel-cell capacity (MW)	16.2	25.3	17.9	45.3
Electrolyser capacity (MW)	46.8	48.1	47.1	51.2
Compressor capacity (kg/h)	955.6	1068.0	961.2	1136.0
HSS-converter capacity (MW)	50.2	51.5	50.5	54.8
Additional converter capacity (MW)	N/A	N/A	3.0	5.2
Storage-tank capacity (kg)	4404.5	5125.4	4131.5	5620.9
Target footroom M_{ft}^{STR} (kg)	1445.1	2713.8	1730.3	4117.7
Target headroom M_{hd}^{STR} (kg)	2385.0	Ineffective	Ineffective	Ineffective
Limit for discharge M_{dis}^{STR} (kg)	N/A	N/A	2714.2	4988.3
Limit for charge M_{ch}^{STR} (kg)	N/A	N/A	2940.5	4106.7

in a reasonable storage headroom for the HF provision for most of the time.

Since the maximum OB magnitudes cannot restore 20% of the MER in a SP as required by the SOE rules, the HSS is suggested here to take the risk of penalties on DR under-delivery rather than using an excessively large electrolyser and fuel cell to comply with the SOE rules. Despite the limited OB magnitudes, the storage-tank capacity optimized for 2030 or 2050 is much greater than the associated MER for DR market entry (i.e. 1828.6 kg for 2030 or 2367 kg for 2050 under the NPE, or 1945.5 kg for 2030 or 3419.7 kg for 2050 under the PE), providing sufficient room for H_2 storage variations for the majority of the time. Furthermore, the target H_2 storage footroom that guides the (importing) OB for H_2 recovery is shown to accordingly increase with the LF capacity. In addition, the H_2 storage limit M_{dis}^{STR} on the fuel-cell export to wind-farm meter in the PE configuration is optimized to be very close to or even exceed the limit M_{ch}^{STR} for the absorption of wind curtailment. This indicates less incentive for the HSS to implement a large-scale time shift of wind generation at the same time as the DR provision in this study, though the power interchange with the wind farm via the additional converter enables the HSS to additionally manage its H_2 storage level.

3.2 DR delivery performance

Fig. 6 compares the DR responses delivered by the optimized co-location system in the NPE or PE under the 2030 or 2050 scenario with the DR response curve, respectively. The HSS co-location system is shown to mostly follow the DR curve, though a number of under-delivery events are observed in each direction (especially for LF DR) due to the storage tank being fully discharged or charged. Fig. 7 shows the distributions of state of charge (SOC) levels of the storage tank under different operating scenarios. Compared with the 2030 scenarios, the percentage of time that the SOC falls below 1% or exceeds 99% is reduced under the 2050 scenarios due to the use of a larger storage tank and a greater OB magnitude for H_2 recovery (see Table 3). In addition, the occurrence of extreme SOC events is slightly alleviated in the PE configuration due to the additional storage management via the power interchange with the wind farm. As shown in Fig. 6, a full storage tank leads to HF responses falling to zero, whereas the LF responses in the events of an empty storage tank generally drop to a specific level equalling the maximum magnitude of the (importing) OB plus the additional converter capacity (if available). This is because the HSS would follow the maximum allowable OB magnitude to replenish the empty storage tank and, if in the PE configuration, require the wind farm to support the LF delivery subject to the available wind power and the additional converter capacity.

The distributions of the resulting maximum percentage errors of LF and HF responses in EFA blocks are shown in Fig. 8, respectively. As was depicted by Equation (23), a maximum percentage error within 5% will not cause a penalty on DR under-delivery, whereas a maximum percentage error exceeding 25% will induce a full deduction in the DR payment. Therefore, according to the maximum percentage errors in Fig. 8, the co-location system can receive full DR payments in the majority of the EFA blocks and occasionally suffer from a full payment deduction (especially for LF DR) in some particular EFA blocks. In addition, Fig. 8 shows that the use of the PE configuration achieves a better performance in DR delivery on average than the NPE configuration, mainly due to the support of the wind farm in LF events and the additional storage management enabled by the additional converter.

3.3 Co-location system operation

The optimization-based system operation over four particular EFA blocks in the PE configuration under the 2030 scenario is shown in Figs 9–11 to reflect the effectiveness of the operating strategy designed here, including the DR delivery on the basis of the submitted OB, the interaction between HSS components and their coordination with the wind farm. Since the H_2 storage prediction $M_{i+2,T}^{STR}$ at the end of the SP (i + 2) is smaller than the target footroom level throughout the first EFA block (see Fig. 9), the negative OBs with a magnitude of 0.5 MW (i.e. the maximum allowable magnitude as was noted in Section 3.1) are submitted and followed by the HSS for H_2 recovery, as shown in Fig. 10. However, the magnitude of the negative OB is so small that the H_2 storage prediction $M_{i+2,T}^{STR}$ is very close to the present storage level (see Fig. 9). Driven by the grid frequency signal, the required DR response is added onto the OB, with their aggregate being completely followed by the power flow across the HSS meter in Fig. 10. Furthermore, Fig. 10 shows that the power flows across the HSS meter are greater than the fuel-cell export in some events, e.g. 2778–2778.5 hours, with the exceedances being contributed by the otherwise curtailed wind power P_{WF}^{HSS}

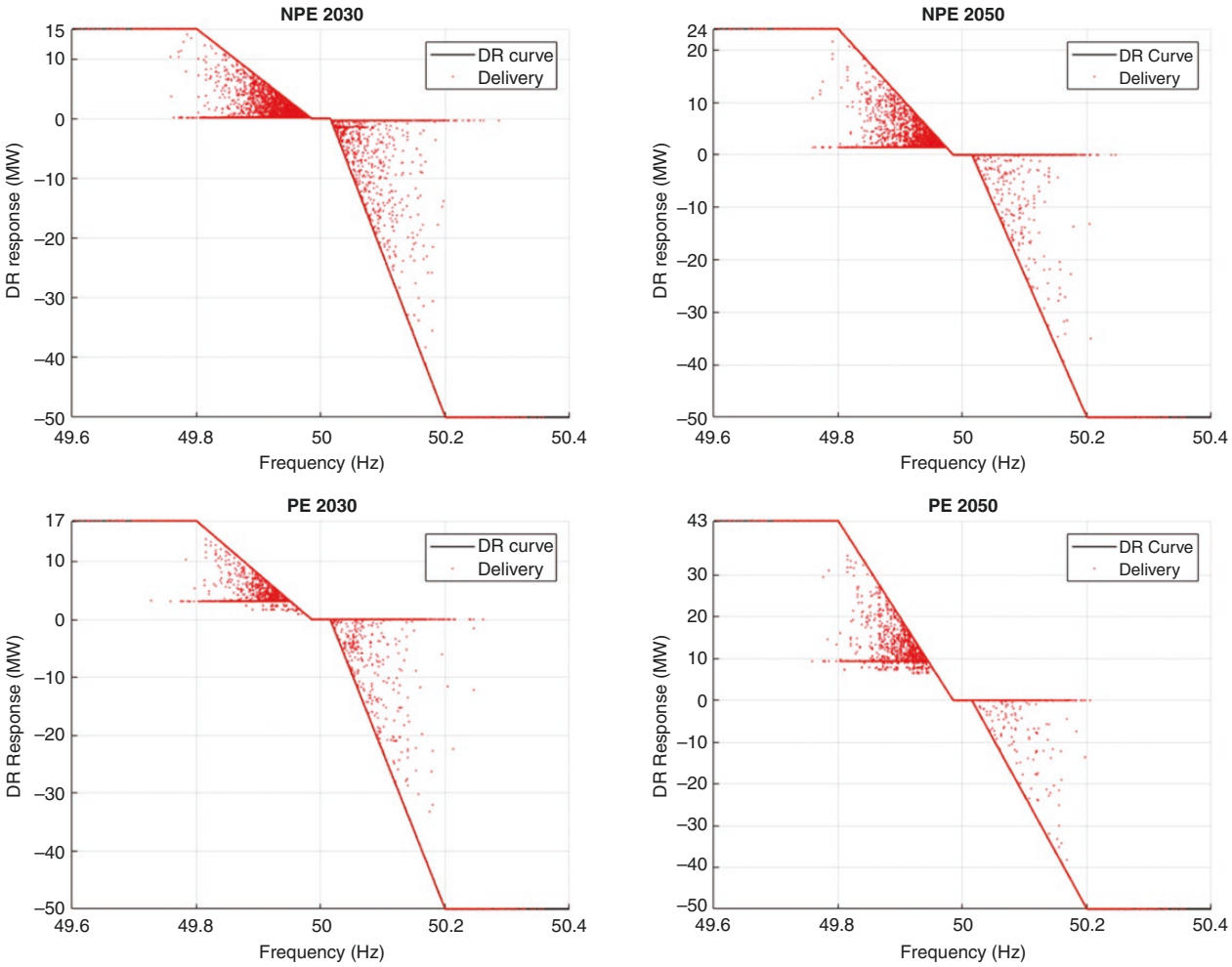

Fig. 6: DR response curves against actual DR delivery (MW) by the system in NPE or PE under 2030 or 2050 scenario.

(see Fig. 11) when the predictions $M^{STR}_{i+2,T}$ are below the limit for charging (see Fig. 9); given the additional converter capacity being not exhausted by P^{HSS}_{WF}, the additional wind power P^{E+C}_{WF} that would otherwise be curtailed is transferred across the additional converter (see Fig. 11) and imported by the electrolyser and compressor (see Fig. 10) for H_2 production and pressurization. However, it is noted that the delivery of LF responses still aggravates the wind curtailment in this high-wind period since only a small part of the wind curtailment can be exploited by the HSS side given the limited additional converter capacity. In addition, Fig. 10 shows that the compressor consumption is much smaller than the corresponding electrolyser import, only accounting for ~1.82% of their aggregate power input in this case.

Since the transfer of P^{HSS}_{WF} and P^{E+C}_{WF} to the HSS side reduces the H_2 consumption for fuel-cell export to the HSS meter and provides free electricity to the electrolyser and the compressor for H_2 recovery, respectively, Fig. 9 shows that the H_2 storage level gradually increases towards and eventually exceeds the limit for discharging at 2780.5 hours. With the available wind-power output falling below the connection ampacity after 2782 hours (see Fig. 11), the headroom in connection ampacity allows the fuel cell to consume the surplus of H_2 above the discharging limit when neither DR responses nor OBs would import electricity from the main grid, as was noted in Section 1.4.2. Fig. 10 shows that the fuel-cell outputs are greater than the non-negative power transfers flowing to the HSS meter after 2782 hours, with the exceedance of P^{sell}_{HSS} being delivered to the wind-farm meter subject to the additional converter capacity (see Fig. 11). This not only helps manage the H_2 storage level to keep the storage headroom for HF events, but could also bring additional revenue to the co-location system through the imbalance prices.

3.4 Cost–benefit analysis

The cumulative present values of different revenue and cost items of the optimized co-location systems in NPE and PE configurations under 2030 and 2050 scenarios are tabulated in Table 4, respectively. Among a variety of HSS components, the electrolyser and the fuel cell make the main contributions to the overall CAPEX and OPEX of the HSS. Although greater electrolyser capacities are employed in the 2050 scenarios, their costs are smaller than those for the 2030 scenarios due to the decreased unit price. Furthermore, given that the stacks of the electrolyser and the fuel cell would be replaced once in a 15-year project lifespan, their stack-replacement costs are also considerable and vary with the CAPEX of the electrolyser and the fuel cell and the time that the replacement occurs. In addition, the growth of connection

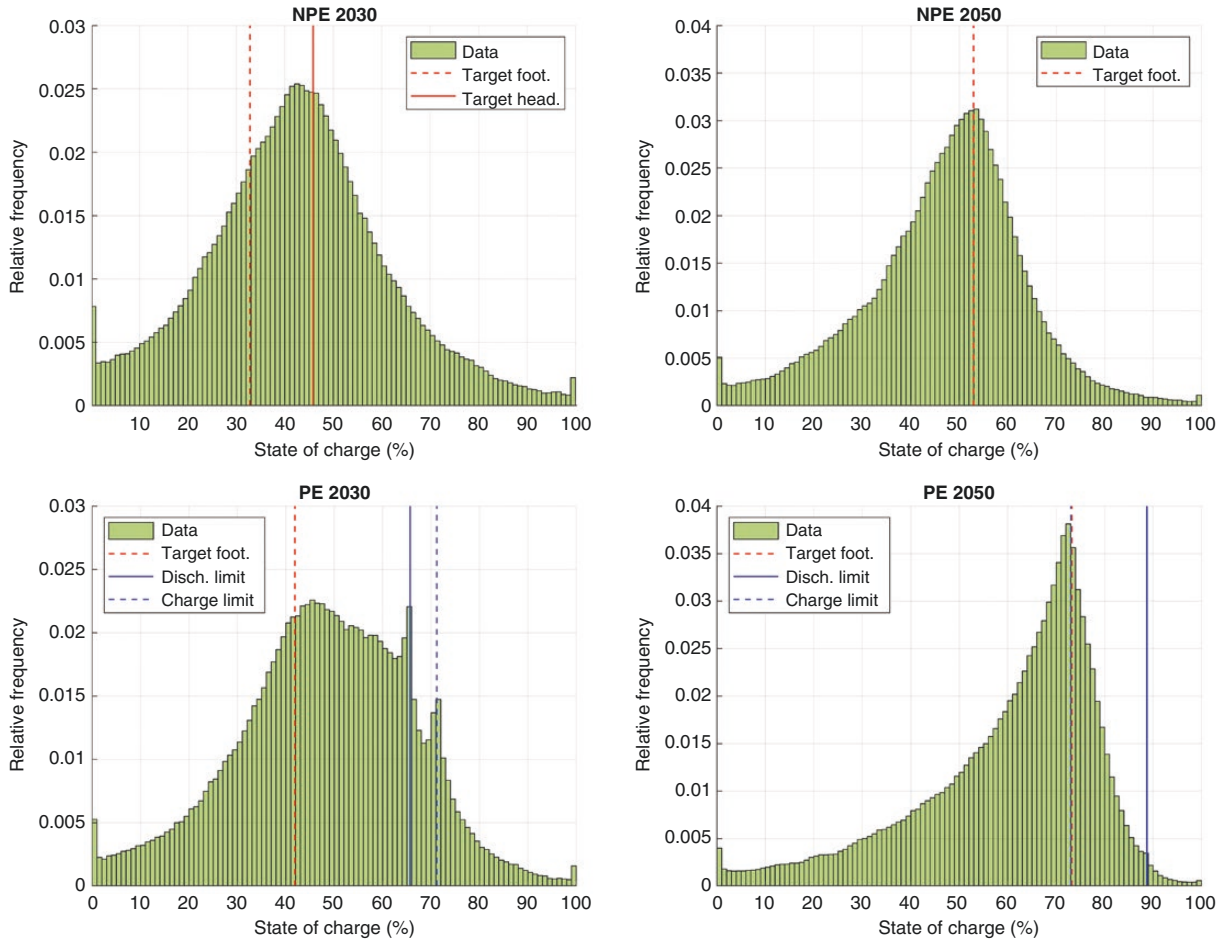

Fig. 7: Relative frequencies of state of charge levels (%) of H_2 storage tank in NPE or PE under 2030 or 2050 scenario.

charges and the cost of external freshwater import (especially the latter) are much smaller than those of HSS assets.

Despite the huge expenses for the HSS placement and operation, the provision of DR services by the HSS brings significant revenue to the co-location system. The higher LF DR capacity contracted in the PE configuration and/or under the 2050 scenario (see Table 3) results in greater availability payments for the LF provision. As was noted in Section 3.1, the maximum magnitude of the (importing) OB for H_2 recovery increases with the LF capacity, which increases the OB-related electricity costs. Since the HSS in the NPE-based 2030 scenario provides a LF capacity of 15 MW only and allows an (exporting) OB of ≤0.4 MW for H_2 release, it is shown to receive the revenue from OBs on average. Furthermore, the provision of a higher LF DR capacity increases the LF responses and aggravates the wind curtailment, not only causing a greater reduction in the green subsidy, but also increasing the EICs paid by the wind farm. In addition, since the HF DR capacity of 50 MW is greater than the LF capacity, the system is required to pay the EICs for DR responses on average. In general, the overall EICs paid by the co-location system are reduced with the increased LF DR capacity and by the selection of the PE configuration where the surplus of H_2 can be consumed by the fuel cell to provide additional export to the wind-farm meter.

Given the significant revenue of the DR service provision, Table 4 shows that the co-location system can achieve a positive NPV at the end of the project lifespan with an internal rate of return (IRR) of ≥15% in all the cases. With the unit price drops of the electrolyser and the fuel cell and the increase in the contracted LF DR capacity, the 2050 scenarios lead to greater final NPVs and higher IRRs than the 2030 scenarios. In addition, compared with the NPE configuration, the use of the PE configuration along with its associated operating strategy increases the final NPV by ~3.9% and ~6.5% under 2030 and 2050 scenarios, respectively, though the IRR is slightly reduced in the PE-based scenario due to the increased one-off investments into HSS assets (especially fuel cells). It is noted that the DR availability payments are evaluated here based on a DR unit price of £20/MWh, which might be overestimated in the future DR service market. To understand the possible minimum tendered price that could guide the biddings in DR service auctions, the DR unit price that would lead to a zero NPV (i.e. the resulting DR payment reduction equalling the NPV) is inferred from Table 4. It is estimated that a profitable wind-farm and HSS co-location project would be achieved when the DR unit price is at least around £16.4/MWh or £14.3/MWh in the NPE-based 2030 or 2050 scenario, or £15.4/MWh or £15.1/MWh in the PE-based 2030 or 2050 scenario, respectively.

4 Conclusions

The development of electrolyser and fuel-cell technologies together with the reforms of frequency-response service markets in Great Britain have increased the techno-economic feasibility

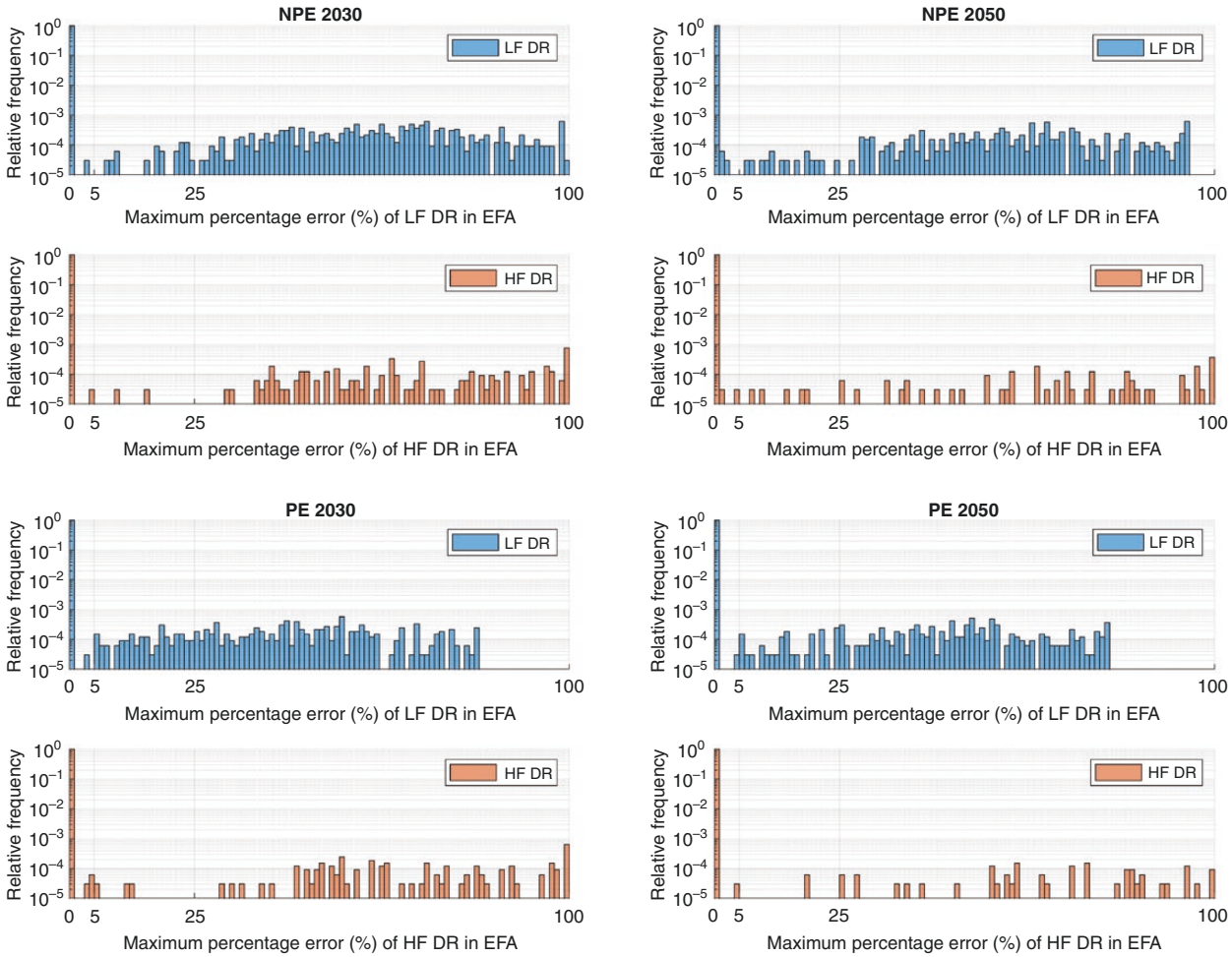

Fig. 8: Relative frequencies of maximum percentage errors (%) of LF and HF DR responses in EFA blocks for the system in NPE or PE under 2030 or 2050 scenario.

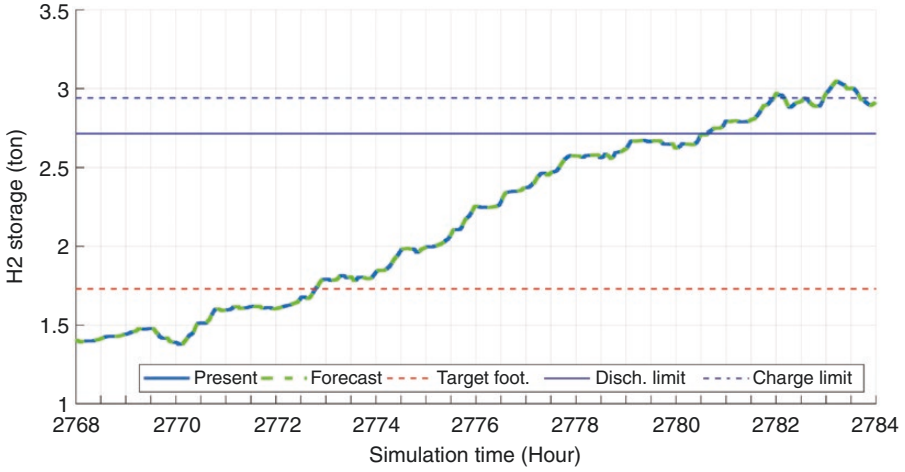

Fig. 9: The profiles (ton) of present H_2 storage levels and predictions at the end of the SP (i + 2) against the target footroom level and the storage limits for discharging and charging over 2768–2784 hours in the PE configuration under the 2030 scenario.

of developing a HSS to provide frequency-response services. To perform an optimization-based assessment on the profitability of co-locating an HSS with a wind farm for frequency-response provision, this paper has developed a modelling framework to simulate the techno-economic operation of a wind-farm and HSS co-location system that delivers DR frequency responses to Great Britain's transmission system. The interaction between HSS components and their coordination with a wind farm have been modelled by respecting the DR market mechanisms, the balance of power and hydrogen (H_2) flows, as well as their mutual conversion.

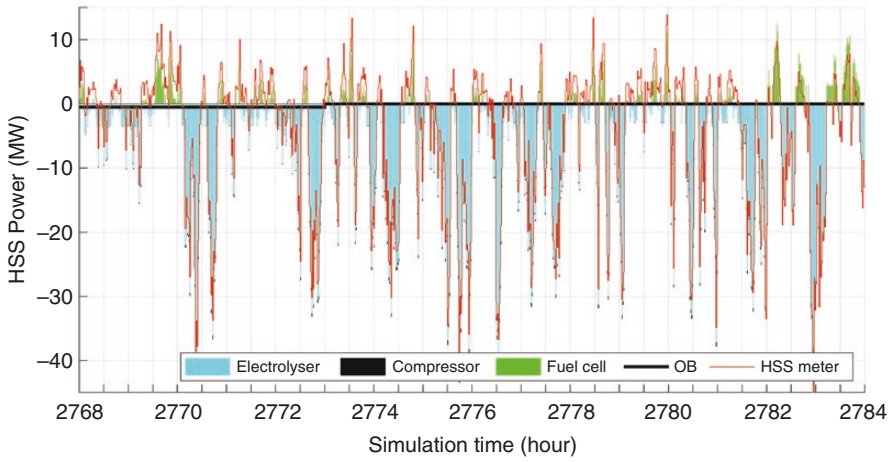

Fig. 10: The profiles (MW) of power inputs of the electrolyser and compressor and outputs of the fuel cell against OBs and power flows across the HSS meter over 2768–2784 hours in the PE configuration under the 2030 scenario.

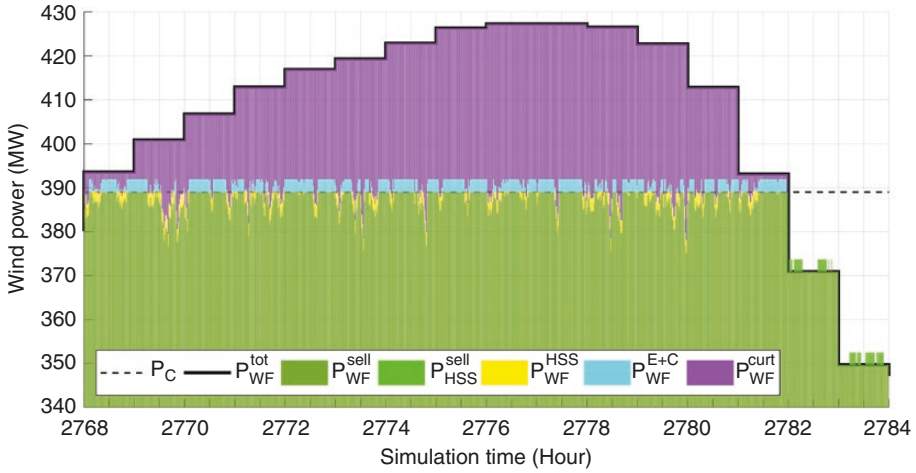

Fig. 11: The profiles (MW) of available wind-power outputs P^{tot}_{WF}, wind export P^{sell}_{WF} and HSS export P^{sell}_{HSS} across the wind-farm meter, wind export across the HSS meter P^{HSS}_{WF} or imported by electrolyser/compressor P^{E+C}_{WF} and wind curtailment P^{curt}_{WF} over 2768–2784 hours in the PE configuration under the 2030 scenario.

Then the techno-economic simulation of the co-location system have been combined with a PSO method to maximize the system's NPV by optimizing the capacities of different HSS components, LF and HF DR capacities, and H_2 storage-related strategy variables that guide the OB submission for H_2 restoration and the power interchange between the wind farm and the HSS.

The effectiveness of the modelling framework has been tested in the context of a particular 432-MW wind farm in Great Britain based on the techno-economic characteristics of HSS components projected for 2030 and 2050. The optimization has suggested that the co-location system can provide the maximum allowable HF capacity combined with a LF-to-HF capacity ratio close to the round-trip efficiency of the HSS. When an additional converter is employed to enable the power transfer between the wind-farm and HSS sides, a higher LF-to-HF capacity ratio has been achieved due to the support of the wind farm in LF responses at times of wind curtailment and/or insufficient H_2 storage. Furthermore, the HSS has been suggested to take the risk of penalties on DR under-delivery rather than employing excessively large electrolysers and fuel cells to comply with the SOE rules. In addition, the incentive for the HSS to perform the time shift of wind generation via the additional converter is mitigated by the DR provision in this study, though the power interchange with the wind farm could help the HSS to additionally manage its H_2 storage level. Given a DR unit price of £20/MWh, the significant revenue of the DR provision has compensated for the considerable investments and ongoing costs of the HSS and other revenue losses induced by the HSS operation, resulting in a profitable HSS co-location project under both 2030 and 2050 scenarios.

Building on the present work, the hot standby modes and detailed degradation mechanisms of the electrolyser and the fuel cell should be introduced into the modelling framework. Furthermore, the modelling framework will be extended to explore the techno-economic feasibility of deploying an HSS to stack the revenue streams of DR service provision and local H_2 supply. In addition, the values of the by-product oxygen from the electrolyser will be evaluated. The comparison in profitability between the stacking of different revenue streams can help wind-farm developers to identify the best business model for an HSS co-location project.

Table 4: Cumulative present values (k£) of monetary items of co-location systems in NPE and PE under 2030 and 2050 scenarios

Variable	NPE		PE	
	2030	2050	2030	2050
Fuel-cell CAPEX (k£)	–10 089.7	–12 550.5	–11 179.8	–22 486.4
Electrolyser CAPEX (k£)	–28 208.2	–23 177.8	–28 373.8	–24 652.3
Compressor CAPEX (k£)	–2194.0	–2197.3	–2202.5	–2288.5
Converter CAPEX (k£)	–3766.7	–3860.7	–4010.1	–4495.8
Storage-tank CAPEX (k£)	–1941.5	–2259.3	–1821.2	–2477.7
Overall HSS OPEX (k£)	–12 753.5	–13 073.0	–13 381.9	–18 741.0
Stack-replacement cost (k£)	–6312.0	–5512.5	–6603.6	–8119.6
H_2O import cost (k£)	–228.5	–237.4	–240.0	–321.1
δ connection charge (k£)	–1248.3	–1446.3	–1286.1	–1935.0
LF DR payment (k£)	22 981.9	36 957.3	26 183.8	66 322.8
HF DR payment (k£)	77 379.8	77 528.2	77 450.3	77 602.9
OB-related (k£)	283.4	–3484.6	–648.4	–13 776.9
δ green subsidy (k£)	–2109.5	–2821.3	–2316.1	–4537.4
δ EIC (k£)	–13 841.3	–11 022.9	–12 913.4	–5103.7
NPV (k£)	17 961.9	32 841.8	18 657.3	34 990.3
IRR (%)	15%	22%	15%	20%

Acknowledgements

This work was conducted as part of the research programme of the Electrical Infrastructure Research Hub in collaboration with the Offshore Renewable Energy Catapult and the University of Strathclyde. F.F.: conceptualization, data curation, formal analysis, investigation, methodology, software, validation, visualization, writing—original draft preparation. S.S.: formal analysis, investigation, methodology, software, validation, visualization, writing—review and editing. D.C.-G.: conceptualization, funding acquisition, investigation, project administration, resources, supervision, validation, writing—review and editing. J.N.: conceptualization, funding acquisition, investigation, project administration, supervision, validation, writing—review and editing.

Conflict of interest statement

None declared.

References

[1] International Energy Agency. *Technology Roadmap: Hydrogen and Fuel Cells*. https://www.iea.org/reports/technology-roadmap-hydrogen-and-fuel-cells (7 September 2022, date last accessed).

[2] International Renewable Energy Agency. *Hydrogen from Renewable Power: Technology Outlook for the Energy Transition*. https://www.irena.org/publications/2018/sep/hydrogen-from-renewable-power (28 September 2022, date last accessed).

[3] Oni AO, Anaya K, Giwa T, *et al*. Comparative assessment of blue hydrogen from steam methane reforming, autothermal reforming, and natural gas decomposition technologies for natural gas-producing regions. *Energy Conversion and Management*, 2022, 254:115245.

[4] Coutanceau C, Baranton S, Audichon T. *Hydrogen Electrochemical Production*. London: Academic Press, 2017, 17–62.

[5] International Renewable Energy Agency. *Hydrogen: A Renewable Energy Perspective*. https://www.irena.org/publications/2019/Sep/Hydrogen-A-renewable-energy-perspective (9 September 2022, date last accessed).

[6] Stamatakis E, Perwog E, Garyfallos E, *et al*. Hydrogen in grid balancing: the European market potential for pressurized alkaline electrolysers. *Energies*, 2022, 15:637.

[7] National Renewable Energy Laboratory. *Novel Electrolyzer Applications: Providing More than Just Hydrogen*. https://www.nrel.gov/docs/fy14osti/61758.pdf (26 November 2022, date last accessed).

[8] Allidieres L, Brisse A, Millet P, *et al*. On the ability of PEM water electrolysers to provide power grid services. *International Journal of Hydrogen Energy*, 2019, 44:9690–9700.

[9] You S, Reissner R, Imboden C, *et al*. Facilitating water electrolysers for electricity-grid services in Europe through establishing standardized testing protocols. *Clean Energy*, 2020, 4:379–388.

[10] Ewan M, Rocheleau R, Swider-Lyons K, *et al*. Development of a hydrogen energy system as a grid frequency management tool. *ECS Transactions*, 2016, 75:403–419.

[11] Mohanpurkar M, Luo Y, Terlip D, *et al*. Electrolyzers enhancing flexibility in electric grids. *Energies*, 2017, 10:18361836.

[12] Matute G, Yusta JM, Correas LC. Techno-economic modelling of water electrolysers in the range of several MW to provide grid services while generating hydrogen for different applications: a case study in Spain applied to mobility with FCEVs. *International Journal of Hydrogen Energy*, 2019, 44:17431–17442.

[13] Larscheid P, Luck L, Moser A. Potential of new business models for grid integrated water electrolysis. *Renewable Energy*, 2018, 125:599–608.

[14] Dadkhah A, Bozalakov D, De Kooning JDM, *et al*. On the optimal planning of a hydrogen refuelling station participating in the electricity and balancing markets. *International Journal of Hydrogen Energy*, 2021, 46:1488–1500.

[15] Dadkhah A, Bozalakov D, De Kooning JDM, *et al*. Techno-economic analysis and optimal operation of a hydrogen refueling station providing frequency ancillary services. *IEEE Transactions on Industry Applications*, 2022, 58(4): 5171–5183.

[16] Apostolos D. Optimisation of a hydrogen production–storage–re-powering system participating in electricity and transportation markets: a case study for Denmark. *Applied Energy*, 2020, 265:114800.

[17] Alshehri F, Suarez VG, Torres JLR, *et al*. Modelling and evaluation of PEM hydrogen technologies for frequency ancillary services in future multi-energy sustainable power systems. *Heliyon*, 2019, 5:e01396.

[18] Quan X, Hu Q, Dou X, *et al*. Control of grid-forming application for fuel cell/electrolyser system. *IET Renewable Power Generation*, 2020, 14:3368–3374.

[19] Fuel Cells and Hydrogen 2 Joint Undertaking. *Study on Early Business Cases for H2 in Energy Storage and More Broadly Power to H2 Applications*. https://www.fch.europa.eu/publications/study-early-business-cases-h2-energy-storage-and-more-broadly-power-h2-applications (7 September 2022, date last accessed).

[20] Hydrogen and Fuel Cell Technologies Office. *H2A Hydrogen Delivery Infrastructure Analysis Models and Conventional Pathway Options Analysis Results—Interim Report*. https://www.energy.gov/eere/fuelcells/downloads/h2a-hydrogen-delivery-infrastructure-analysis-models-and-conventional (26 September 2022, date last accessed).

[21] Menon ES. *Pipeline Planning and Construction Field Manual*. Oxford: Gulf Professional Publishing, Elsevier Inc., 2011.

[22] INTECH GmbH. *Basic Steps to Compressor Unit Calculation and Selection*. https://intech-gmbh.com/compr_calculation_and_selection/ (8 September 2022, date last accessed).

[23] International Council on Clean Transportation. *Assessment of Hydrogen Production Costs from Electrolysis: United States and Europe*. https://theicct.org/publication/assessment-of-hydrogen-production-costs-from-electrolysis-united-states-and-europe/ (8 September 2022, date last accessed).

[24] International Energy Agency. *The Future of Hydrogen: Seizing Today's Opportunities*. https://www.iea.org/reports/the-future-of-hydrogen (8 September 2022, date last accessed).

[25] Fan F, Zorzi G, Campos-Gaona D, *et al*. Wind-plus-battery system optimisation for frequency response service: the UK perspective. *Electric Power Systems Research*, 2022, 211:108400.

[26] National Grid Electricity System Operator. *Dynamic Regulation Service Terms Version 1.0*. https://www.nationalgrideso.com/document/246761/download (26 September 2022, date last accessed).

[27] National Grid Electricity System Operator. *Dynamic Moderation Service Terms Version 1.0*. https://www.nationalgrideso.com/document/246736/download (26 September 2022, date last accessed).

[28] National Grid Electricity System Operator. *Dynamic Containment Service Terms Version 4.0*. https://www.nationalgrideso.com/document/177106/download (26 September 2022, date last accessed).

[29] National Grid Electricity System Operator. *Dynamic Regulation Participation Guidance Document Version 1.0*. https://www.nationalgrideso.com/document/246751/download (26 September 2022, date last accessed).

[30] Jülch V. Comparison of electricity storage options using levelized cost of storage (LCOS) method. *Applied Energy*, 2016, 183:1594–1606.

[31] Nord Pool. *N2EX Day Ahead Auction Prices*. https://www.nordpoolgroup.com/en/Market-data1/GB/Auction-prices/UK/Hourly/?view=table (28 September 2022, date last accessed).

[32] Department for Business, Energy and Industrial Strategy. *Contracts for Difference: Policy Paper*. https://www.gov.uk/government/publications/contracts-for-difference/contract-for-difference (28 September 2022, date last accessed).

[33] Low Carbon Contracts Company. *Actual CfD Generation and Avoided GHG Emissions*. https://www.lowcarboncontracts.uk/data-portal/dataset/actual-cfd-generation-and-avoided-ghg-emissions (8 September 2022, date last accessed).

[34] Elexon. *The Electricity Trading Arrangements: A Beginner's Guide*. https://www.elexon.co.uk/documents/training-guidance/bsc-guidance-notes/beginners-guide-2/ (28 September 2022, date last accessed).

[35] National Grid Electricity System Operator. *Application Fee Calculator 19_20_0*, 2020. https://www.nationalgrideso.com/document/154976/download (28 September 2022, date last accessed).

[36] National Grid Electricity System Operator. *TNUoS Guidance for Generators*. https://www.nationalgrideso.com/document/138046/download (28 September 2022, date last accessed).

[37] National Grid Electricity System Operator. *Introduction to Balancing Services Use of System Charges (BSUoS)*. https://www.nationalgrideso.com/document/137681/download (28 September 2022, date last accessed).

[38] National Grid Electricity System Operator. *Final TNUoS Tariffs for 2019/20*. https://www.nationalgrideso.com/document/137351/download (28 September 2022, date last accessed).

[39] National Grid Electricity System Operator. *Balancing Services Use of System (BSUoS) Charges*. https://www.nationalgrideso.com/industry-information/charging/balancing-services-use-system-bsuos-charges (28 September 2022, date last accessed).

[40] Kennedy J, Eberhart R. Particle swarm optimisation. In: *Proceedings of ICNN95—International Conference on Neural Networks*, Perth, Australia, 27 November–1 December 1995, 1942–1948.

[41] The MathWorks, Inc. *MATLAB R2018b*. https://www.mathworks.com/help/releases/R2018b/index.html (28 September 2022, date last accessed).

[42] The Crown State. *Round 3 Offshore Wind Farm Connection Study*. https://energy.soutron.net/Library/Download.aspx?id=4629 (28 September 2022, date last accessed).

[43] Staffell I, Pfenninger S. Using bias-corrected reanalysis to simulate current and future wind power output. *Energy*, 2016, 114:1224–1239.

[44] Molod A, Takacs L, Suarez M, *et al*. Development of the GEOS-5 atmospheric general circulation model: evolution from MERRA to MERRA2. *Geoscientific Model Development*, 2015, 8:1339–1356.

[45] National Grid Electricity System Operator. *Historic Frequency Data*. https://www.nationalgrideso.com/industry-information/balancing-services/frequency-response-services/historic-frequency-data (28 September 2022, date last accessed).

[46] Elexon. *System Sell & System Buy Prices*. https://www.bmreports.com/bmrs/?q=balancing/systemsellbuyprices (28 September 2022, date last accessed).

[47] Department for Business, Energy and Industrial Strategy. *Capacity of UK Electricity Generation Assets in the 21st Century, 2000 to 2019*. https://www.gov.uk/government/publications/energy-trends-march-2021-special-feature-article-capacity-of-uk-electricity-generation-assets-in-the-21st-century-2000-to-2019 (11 December 2022, date last accessed).